Comparing advanced-era interferometric gravitational-wave detector network configurations: Sky localization and source properties

Mattia Emma⬤,[*] Tiago Fernandes de Nobrega⬤, and Gregory Ashton⬤

Department of Physics, Royal Holloway, University of London, Egham, TW20 0EX, United Kingdom

The expansion and upgrade of the global network of ground-based gravitational-wave detectors promises to improve our capacity to infer the sky localization of transient sources, enabling more effective multimessenger follow-ups. At the same time, the increase in the signal-to-noise ratio of detected events allows for more precise estimates of the source parameters. This study aims to assess the performance of advanced-era networks of ground-based detectors, focusing on the Hanford, Livingston, Virgo, and KAGRA instruments. We use full Bayesian parameter estimation procedures to predict the scientific potential of a network. Assuming a fixed configuration of the LIGO Hanford and Livingston detectors, we find that the addition of the Virgo detector is beneficial to the sky localization starting from a binary neutron star range of 20 Mpc and improves significantly from 40 Mpc onward for both a single and double LIGO detector network, reducing the inferred mean sky area by up to 95%. Similarly, the KAGRA detector tightens the constraints, starting from a binary neutron star range of 10 Mpc. Looking at highly spinning binary black holes, we find significant improvements with increasing sensitivity in constraining the intrinsic source parameters when adding Virgo to the two LIGO detectors. Finally, we also examine the impact of the low-frequency cutoff data on the signal-to-noise ratio. We find that existing 20 Hz thresholds are sufficient and propose a metric to monitor this to study detector performance. Our findings quantify how future enhancements in detector sensitivity and network configurations will improve the localization of gravitational-wave sources and allow for more precise identification of their intrinsic properties.

I. INTRODUCTION

The detections of the first binary black hole (BBH) GW150914 [1] and binary neutron star (BNS) GW170817 [2], gravitational-wave signals have been major discoveries opening a new window into our Universe. They not only allowed for the confirmation of Einstein's theory of general relativity at an unprecedented level of accuracy [3–5], but also deepened our knowledge of the physics of compact objects [6–9] and the evolutionary history of the Universe [10]. These scientific breakthroughs were only possible thanks to the highly sophisticated network of ground-based gravitational-wave interferometers developed by the LIGO Scientific [11], Virgo [12], and KAGRA [13] Collaborations. The progressive development of the detectors in the past decades has allowed for a continuous increase in the detection rate throughout the first three observing runs [14–16]. This trend is expected to continue in the current fourth observing run (O4) and beyond, as detector upgrades and the development of next-generation instruments [17–19] promise further advancements in sensitivity and precision.

When considering networks of ground-based gravitational-wave interferometers, one of the metrics used to quantify their performance for transient sources is the sky-localization accuracy obtained through triangulation [20]. Constraining the position of the source of a detected signal improves our understanding of the different populations of compact objects, shedding light onto their distribution across the Universe [21–23]. It also improves the multimessenger follow-up capability [24,25]. The coincident detection of GW170817, GRB170817A, and AT2017gfo [26,27] showed the incredible potential of multimessenger detections, allowing for determining the origin of γ-ray bursts, producing an independent measurement of the Hubble constant [10,28,29] and enhancing our knowledge of the synthesis of heavy elements [30,31]. While GW170814 [32] was the first triple detector event, demonstrating the improvements in sky localization from a three-detector network, the impact of Virgo on the multimessenger follow-up of GW170817 was crucial. Despite the fact that Virgo was not as sensitive as the LIGO detectors, the additional data enabled a significant

---

[*]Contact author: mattia.emma@ligo.org

reduction in the sky-localization area and improved precision of the source parameter estimates [2]. Future detections of multimessenger counterparts could greatly improve our constraints on the neutron star equation of state [8] (e.g., Koehn *et al.* [33] for a review) and our understanding of the formation and evolution of binary black holes [34–37]. To evaluate the electromagnetic follow-up capability, it is important to consider that the field of view of current optical telescopes ranges from 35 deg^2, with an R band sensitivity of $\sim$20 mag, for the Zwicky Transient Facility [38,39] to the 9.6 deg^2 at $\sim$24.5 mag for the Vera Rubin Telescope [40–42].

In this work, we quantify the benefits of having a three- or four-ground-based detector network, including KAGRA and Virgo, compared to the sole LIGO detectors, focusing on the refinements in source-localization accuracy. Starting with Jaranowski *et al.* [43], several authors have worked on the estimation of sky localization and, more generally, parameter estimation accuracy for different networks of detectors for compact binary coalescences. Schutz [20] introduced three figures of merit to compare the performance of networks of detectors. Fairhurst [44,45] then focused on analytically computing the improvements in sky-localization constraints using triangulation from the timing information. Berry *et al.* [46] then looked at the results obtained with this method for different networks of detectors and compared them to parameter estimation ones. Nissanke *et al.* [42] first employed Bayesian methods to compare networks of second-generation ground-based detectors, including a possible detector in Australia [47]. Successive works have either focused on using a limited amount of information to determine the sky localization [48] or on quantifying improvements for specific networks once the component detectors have reached design sensitivity [49–54]. Singer *et al.* [55] first looked at the impact of the Virgo detector on the Hanford-Livingston network. Veitch *et al.* [50] and Shukla *et al.* [54] investigated the improvements related to the addition of the planned LIGO India detector to the current generation of detectors. Furthermore, some studies have concentrated on evaluating the best locations for the third-generation ground-based detectors [56–59]. Other studies have looked at the sky localization and parameter estimation for gravitational-wave burst events [60–64]. Here, we specifically investigate the enhancements facilitated by the inclusion of the Virgo and KAGRA detectors at the sensitivity levels projected for O4 and the fifth observing run (O5) [65,66] for compact binary coalescences.

However, sky localization is not the only improvement one obtains from a better network. We also expect to see improvements in measurements of the source parameters. Most of the signals detected to date originate from black hole binaries with low spin magnitudes ($\chi_i \lesssim 0.4$), aligned spins, and comparable mass components ($q \geq 0.5$) [23]. These results would favor theories that suggest an isolated evolution scenario [67–69] as the main formation channel of black hole binaries [70]. According to this model even if after their formation the black holes have misaligned spins, their unhindered evolution and interaction would lead to a progressive alignment of the spins on timescales much shorter than the merger time. The support for precession, high mass ratios, and high spin magnitudes in the analysis of events such as GW190412 [71] (highly asymmetric masses), GW190814 [72] (highly asymmetric masses), GW190521 [73,74] (high total mass and high spin magnitudes), and GW200129_065458 [75,76] (high spin magnitudes and precession), hereafter referred to as GW200129, has challenged the models for the formation of compact-object binaries [77] and hinted at a connection between precessing systems and high mass ratios. Alternative formation channels for these systems include dynamical formation [78,79], in environments with high stellar density, hierarchical mergers [80,81], and chemically homogeneous evolution [82–84]. Unfortunately, the accuracy in the determination of precession and the intrinsic source parameters, e.g., masses, spins, and their combinations have been limited by the difficulties in producing precise waveform approximants in the region of the multidimensional parameter space where high spins and high mass ratios intersect [76,85–89] and by the signal-to-noise ratio with which we detect the signals [90–93].

In this work, we vary the BNS range of the Virgo and KAGRA detectors and compare how these add to the network performance, assuming a fixed LIGO BNS range. Throughout this study, we refer to the different networks of detectors using abbreviations derived from the initial letters of the included interferometers' names and to the BNS range as the volume- and orientation-averaged distance at which a coalescence gives a matched-filter signal-to-noise ratio of 8 in a single detector [94]. For instance, HL refers to the Hanford and Livingston detectors, following the convention from Abbott *et al.* [51]. In Sec. II, we detail the simulation methodology and the postprocessing procedure to perform full parameter estimation and infer the relevant parameters for our analysis. In Secs. III and IV, we present the results of the evolution of the sky-localization area, while varying the BNS range of one of the detectors in the specific network for BBH and BNS gravitational-wave signals, respectively. We limit our study to the Hanford-KAGRA (HK), Hanford-Virgo (HV), Hanford-Livingston-KAGRA (HLK), Hanford-Livingston-Virgo (HLV), and Hanford-Livingston-Virgo-KAGRA (HLVK) detector networks. We include the two-detector networks to account for the variable duty factor of the single interferometers, which could result in only a subgroup of detectors of the available network being on duty at the time an event happens [95,96]. In Sec. V, we look at the changes in the parameter estimation results for a high-spin BBH merger, emulating the spin magnitude values of GW200129 [76]. Finally, we study the minimum-frequency cutoff in Sec. VI.

The signal-to-noise ratio of detected events, which determines the accuracy of source-parameter estimates, is limited not only by the sensitivity of the detectors, but also by the duration of the signal falling inside the detector's sensitivity bandwidth. The lower cutoff frequency for the data used in the parameter estimation of events detected during the third observing run was typically 20 Hz [16,97], a decision made to balance gains against exponentially increased analysis times. In Sec. VI, we investigate this choice of minimum frequency and develop a metric to quantify the loss of signal-to-noise ratio. We then apply this to data from the third observing run and to simulated data for future BNS range values of the Virgo detector. Finally, in Secs. VII and VIII, we discuss and summarize our results.

II. SIMULATION SETUP

Our objective is to simulate the parameter estimation of gravitational-wave signals by fully replicating the process involved in a real event excluding the impact of glitches, i.e., non-Gaussian transient noise. We add simulated signals to simulated colored Gaussian noise generated from a power spectral density (PSD). Two methods are generally employed to obtain PSD curves in the literature. The first method utilizes actual detector data, as done with the data from the first three observing runs [51]. The second method consists of computing and combining analytical noise curves for different sources influencing each considered detector [12]. Notably, the latter method allows for the simulation of PSDs for future detectors and upgraded versions of current detectors lacking empirical data. These simulations effectively incorporate broken power laws with additional lines, such as those corresponding to the frequency of the power grid coupled to the detector (e.g., 60 Hz in the U.S.) and other known technical noise sources. In this study, we utilize publicly available simulated sensitivity curves for O4 LIGO, KAGRA, and Virgo, as presented in Abbott *et al.* [51]. Specifically, we employ the LIGO O4 high-sensitivity curve with a BNS range of 180 Mpc, the Virgo high-sensitivity curve utilized for O4 simulations with a BNS range of 115 Mpc, and the 25 Mpc KAGRA sensitivity curve, shown in Fig. 1.

To investigate the general trend of sky localization with respect to BNS range, we scale the sensitivity curves to the desired range. To do so, we multiply them by an arbitrary calibration factor until achieving that range with an error lower than 10^{-2}. We determine the BNS range of the sensitivity curve using methods developed by Chen *et al.* [98], simulating an equal-mass binary neutron star with component masses of $1.4 M_\odot$. For KAGRA, we consider BNS range values between 5 and 25 Mpc, while for Virgo, we employ sensitivity curves ranging from 10 to 180 Mpc, approximately covering the expected BNS ranges of the two detectors for future observation runs [51,65,99,100]. Although the scaling method
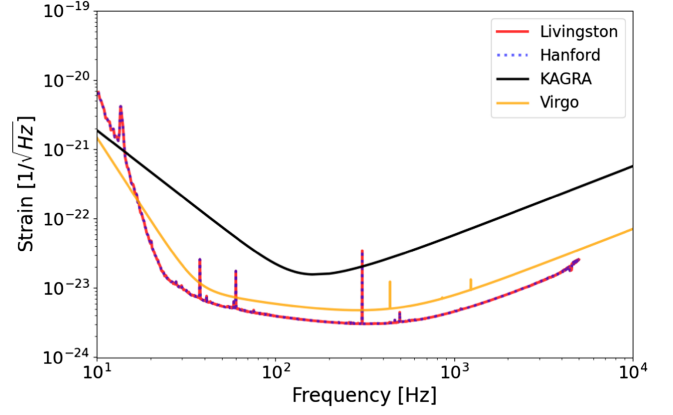

FIG. 1. Comparison of representative sensitivity curves of the detectors employed in our simulations. The overlapping blue dotted and red full lines are the sensitivity curves of the Hanford and Livingston detectors with an optimal BNS range of 180 Mpc. The KAGRA curve, in black, and the Virgo one, in yellow, correspond to BNS detection ranges of 25 and 115 Mpc, respectively. An equal-mass neutron star binary with component masses of $1.4 M_\odot$ was used to compute the BNS range [98].

employed for the spectral density curves provides only an approximation of the real curves, it allows for a first estimate of the performance of the detector networks, which could be refined in the future either with detector curves from real data for the specific BNS range values or using a different scaling for each power law composing the PSD, e.g., a bigger scaling factor at lower frequencies for which the most improvements are expected soon.

Our primary focus is on assessing the impact of the KAGRA and Virgo detectors on the parameter estimation of gravitational-wave signals assuming a fixed O4 LIGO network. To this end, we define the simulated source's location relative to these two additional interferometers and vary only their BNS range while keeping that of the LIGO detectors constant at 180 Mpc. We use the antenna power pattern function $P(\theta, \phi)$ defined in Schutz [20] as

$$\mathrm{P}(\theta,\phi) = \mathrm{F}_+(\theta,\phi,\psi)^2 + \mathrm{F}_\times(\theta,\phi,\psi)^2 \tag{1}$$

$$= \frac{1}{4}(1 + \cos^2\theta)^2\cos^2 2\phi + \cos^2\theta\sin^2 2\psi, \tag{2}$$

where F_+ and $F_\times$ are called the sensitivity functions and θ and ϕ are the spherical coordinates with respect to the detector's axes. We note that the antenna power pattern does not depend on the angle ψ related to the polarization of the gravitational wave. It depends only on the relative orientation of the detector to the source, so that we obtain a wider sky coverage when interferometers are spread across the globe and have maximally different orientations. Table I presents the right ascension (RA), declination (DEC), and single detector antenna pattern function values for the source localizations maximizing and minimizing the

TABLE I. Table of the right ascension, declination, and the values of the single detector's antenna pattern amplitude for the source localization maximizing and minimizing the antenna power pattern function, P_{max} and P_{min}, respectively, for the KAGRA and Virgo detectors. The GPS time is fixed at 1379969683.0.

	RA (rad)	DEC (rad)	P_K	P_V	P_H	P_L
KAGRA P_{max}	1.709	0.761	1.0	0.14	0.22	0.17
KAGRA P_{min}	4.422	0.888	10^{-10}	0.46	0.71	0.80
Virgo P_{max}	5.785	0.761	0.24	1.0	0.17	0.14
Virgo P_{min}	1.392	0.318	0.83	10^{-10}	0.17	0.39

antenna power pattern function for the KAGRA and Virgo detectors. We assume $\psi = 0$ in the computation of the antenna power pattern function values. We show the location and orientation of the current network of ground-based detectors in Fig. 2. We omit the GEO600 [101] detector as we do not include it in our analysis. The large distance between Virgo and KAGRA makes these extremely useful for sky-localization purposes in a four-detector network to obtain precise time-delay measurements.

Furthermore, in Fig. 3 we show 3D visualizations of the antenna power pattern amplitude for the four employed detectors at a fixed GPS time from two different angles. We notice that all detectors have different relative orientations, agreeing with the different antenna pattern values presented in Table I. While the two LIGO detectors are almost parallel, they are orthogonal to KAGRA and Virgo, which are also mutually orthogonal. In this work, we focus on the case in which KAGRA and Virgo have lower sensitivities than the two LIGO detectors. The resulting lower signal-to-noise ratio of detected gravitational-wave events could be partially compensated for some regions of the sky by their different relative orientations. From Table I, we can

compute an estimate of the fraction of LIGO's BNS range at which Virgo and KAGRA data would begin to have an effect on the sky-localization constraints. This corresponds to the quotient between the single LIGO and the Virgo/KAGRA antenna power pattern amplitudes computed at the right ascension and declination values that maximize Virgo/KAGRA's antenna power pattern. For Virgo, we find that the quotient is $\simeq 1/6$, so if the LIGO detectors have a BNS range of 180 Mpc, we would expect to see significant improvements in the sky localization when Virgo reaches sensitivities $\simeq 30$ Mpc. For KAGRA, we find a similar quotient so that we expect improvements from 30 to 35 Mpc onward, values which we do not include in this study. For all the values included in Table I we used the Bilby library [102] to compute the right ascension and declination for the maximum and minimum, respectively, P_{max} and P_{min}, of the antenna power pattern function at a specific arbitrary GPS time for each detector. In Table V in Appendix B, we report the same values for P_{best}, the sky position maximizing the combined detector network antenna power pattern function for each configuration.

Given the source location values, to conduct each analysis we simulate a gravitational waveform and add it to a simulated interferometer data strain to capture the detector's response (see Table II in Appendix A for the simulated parameter values). The process is facilitated using Bilby [102,103]. The colored Gaussian noise background data are simulated from the PSD based on the scaled sensitivity curves, while the added waveform is generated using the LALSimulation library [104]: we employ the IMRPhenomX family of phenomenological waveform models [105]. We use the simulated detector response and waveform to calculate the gravitational-wave transient likelihood [106]. We then provide this likelihood to the Bilby sampler along with priors on relevant parameters, shown in Table III in Appendix A, enabling a
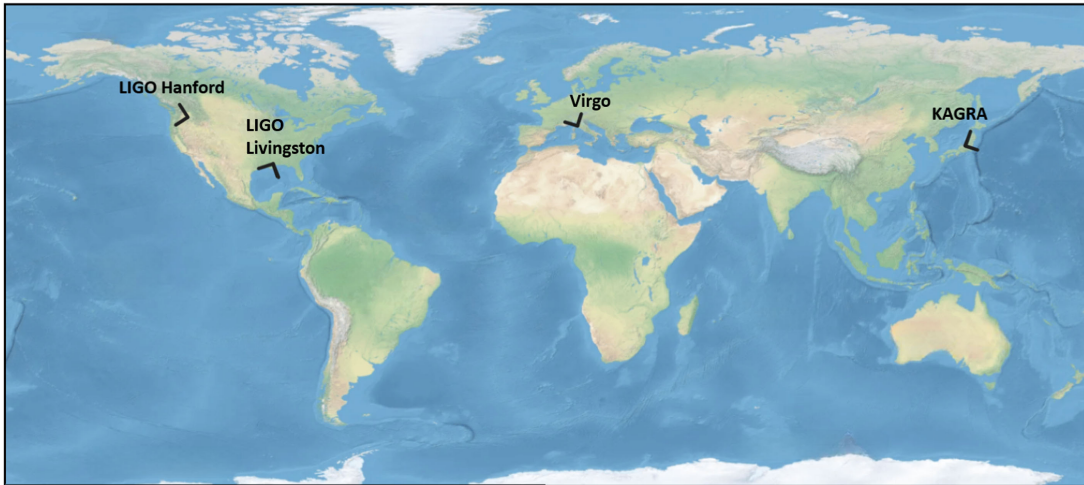

FIG. 2. Location and orientation of the current network of gravitational-wave observatories, identified by the solid black lines. We omit GEO600 as we do not include it in our analysis.
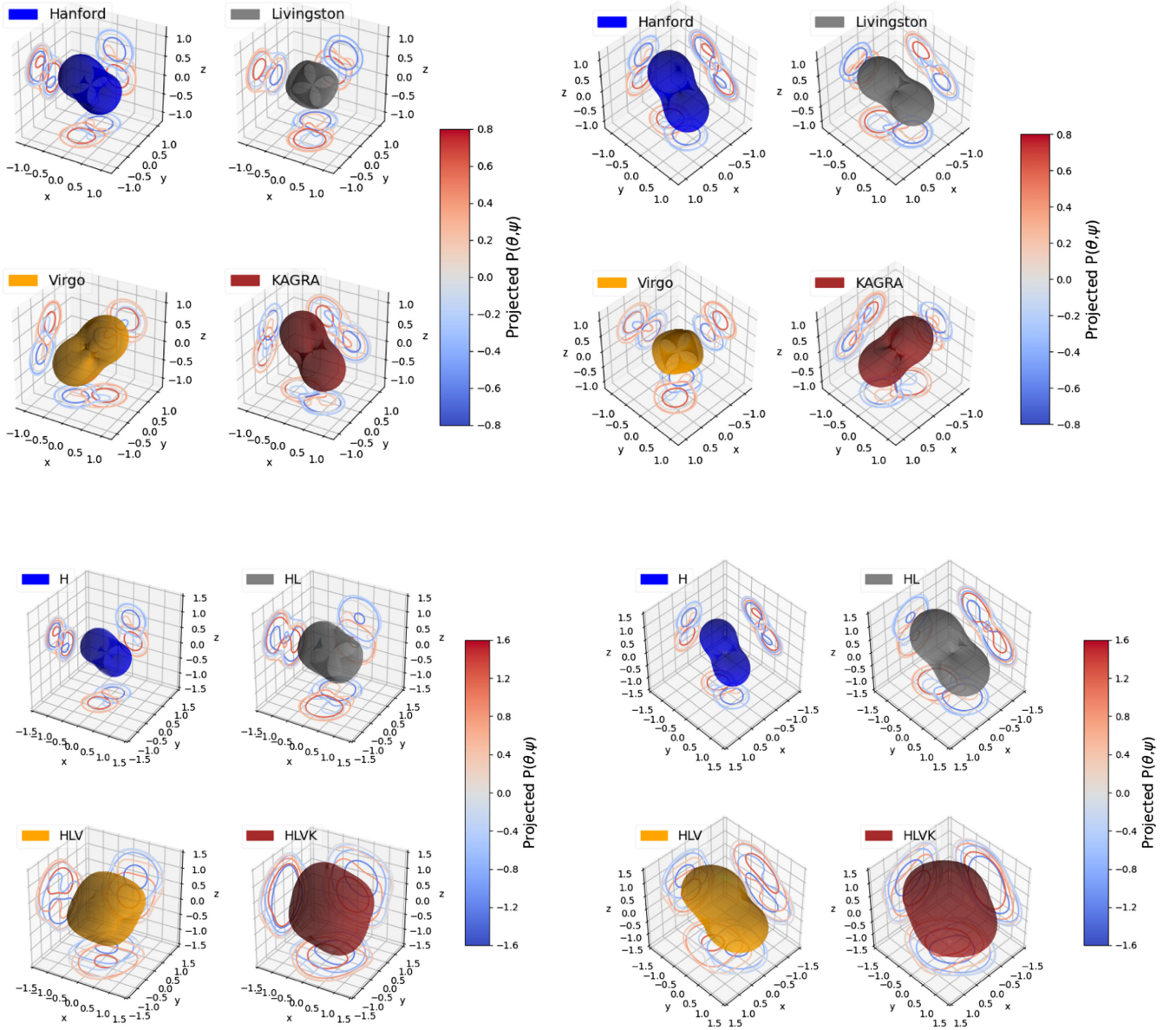
FIG. 3. 3D visualizations of the antenna power pattern amplitude, from Eq. (2), for the LIGO-Hanford, LIGO-Livingston, Virgo, and KAGRA detectors at a fixed arbitrary GPS time, so that the relative orientation of the detectors can be compared. The projections on the two-dimensional planes are the contours of the antenna power pattern amplitude for the projected axis.

comprehensive parameter estimation. We opt for the DYNESTY sampler [107], a nested sampling algorithm [108] that employs differential evolution and adaptive sampling for an effective exploration of the high-dimensional parameter space. We summarize the configuration details for the DYNESTY sampler in Table IV in Appendix A.

A. Postprocessing

For the gravitational-wave signals from highly spinning binary black hole mergers, we want to understand if a larger and more sensitive detector network would allow us to better constrain the source's intrinsic parameters (see Sec. V), while in the nonspinning binary black hole and BNS cases, we want to quantify the improvements in determining the sky localization. We focus on the sky-localization area as we expect it to be influenced the most by adding a new detector to the network [45]. Indeed, the additional detector does not have a comparable or higher BNS range that would enhance the source-parameter estimation results. Nevertheless, its distant location to the LIGO detectors allows for a significant gain in time-delay information which can be used for triangulation purposes. To this end, from the parameter estimation results of the nonspinning system's mergers, we generate a sky map, a graphical representation of the probable source locations of a gravitational-wave event on the celestial sphere. We do this by passing the posterior probability

samples of the distance, right ascension, and declination to the `ligo.skymap` function [109]. Subsequently, we extract the values corresponding to the 90% probability contours of the sky-localization area from the generated sky map. To address the stochastic nature of the sampling process and Gaussian noise and, consequently, the variability in sky-localization area results, we conduct multiple simulations with identical configurations and different realizations of Gaussian noise. By subjecting the obtained pairs of sky-localization and BNS range values to a two-component Gaussian mixture model algorithm, we derive the probability density function (PDF) characterizing the spatial distribution of sky area in relation to BNS range [110]. We chose the two-component model, as it proved to be the best to mirror the distribution of the underlying data, independent of the latter's features. Employing this estimated PDF, we generate 20,000 samples of sky area and BNS range values. Subsequently, we apply a filtering criterion, retaining samples falling within the 5th and 95th percentiles and featuring positive (physical) values for both coordinates. Finally, we classify data points into bins based on the BNS range values, aligning the bin edges with integer values. When varying KAGRA's BNS range, we employ unitary bin widths, while when varying Virgo's BNS range, we use quinary bandwidths.

III. RESULTS OF ZERO SPIN BINARY BLACK HOLE SIMULATIONS

We simulate gravitational-wave signals from nonspinning binary black hole mergers using the IMRPhenomXPHM waveform approximant for both the signal's simulation and the likelihood evaluation [111]. We simulate equal-mass black holes with a detector-frame chirp mass $\mathcal{M}$ of $50M_\odot$, where

$$\mathcal{M} = \frac{(m_1 m_2)^{3/5}}{(m_1 + m_2)^{1/5}}, \qquad (3)$$

with $m_{1/2}$ denoting the detector-frame mass of the two compact objects. The source is placed at a distance of 2000 Mpc from us. The complete list of parameter values can be found in the first column of Table II in Appendix A. Following the procedure outlined in Sec. II, we perform six simulations and full parameter estimation runs for each BNS range value, corresponding to the center of the bins, and postprocess the results into sky-localization area values using a Gaussian mixture model. The results are presented in Fig. 4.

In Fig. 4(a), we show the evolution of the mean and 90% probability contours of the sky area, dots and squares, and shaded area, respectively, for the HL-K detector network varying the BNS range of the KAGRA detector only. Henceforth, we will separate with a dash the letter referring to the detector of the network whose BNS range we have varied for the specific plot. The brown and orange points

and areas were obtained by placing the source in the P_{max} and P_{min} source location, respectively, for the KAGRA detector (see Table I). The black dotted line corresponds to the field of view of the Zwicky Transient Facility. By 0 Mpc we refer to the results obtained with the two LIGO detectors only at a fixed BNS range of 180 Mpc. For all the following sky area plots, we computed the 0 Mpc value with the same detector network used for the other BNS range values but excluding the detector whose BNS range is varied. For Fig. 4(a), while in the P_{max} location case, the mean sky area value decreases notably, when increasing KAGRA's BNS range, it remains roughly constant in the P_{min} location case. The decrease of the mean sky area is most significant from ~10 Mpc onward.

Figure 4(b) shows the sky area results for the P_{max} and P_{min} source locations for the H-K detector network varying the KAGRA BNS range. For the P_{max} case, the sky area improves considerably after ~15 Mpc, with the 90% quantiles spanning to 1 order of magnitude lower values than in the P_{min} case. Also the latter improves slightly from 15 Mpc onward. The mean sky area values for the P_{max} case are of the order 1.5×10^4 deg^2, when KAGRA has a 25 Mpc BNS range, compared to 2×10^4 deg^2 for the P_{min} case. The overall improvement is not significant for precisely localizing the source, and the sky area values are 2 orders of magnitude higher than for the corresponding three-detector network HL-K.

In Fig. 4(c), we report the same quantities as in Fig. 4(a), but for the HL-V detector network, using the P_{max} and P_{min} source location for the Virgo detector. We can see a clear difference between the P_{max} and P_{min} distributions, with the decrease in sky area being almost 2 orders of magnitude more in the former source location case. We notice how the Virgo detector with a BNS range of 35 Mpc and above would provide a significant improvement, reducing the mean sky area to ~10 Mpc. With a Virgo detector BNS range between 25 and 35 Mpc, the inferred sky area improves considerably, although it exhibits a high variability. In the P_{min} case, the improvement in sky area is less remarkable as the mean changes from ~600 deg^2 with the HL detector network to ~250 deg^2 for the LH-V network when Virgo has a BNS range of 100 Mpc.

The corresponding two-detector network, H-V, results are shown in Fig. 4(d). We notice that both the P_{max} and P_{min} distributions follow a similar trend to the ones obtained for the HL-V detector network. In the P_{max} case, we see the most significant improvement in sky area for BNS range values between 25 and 45 Mpc. In this range, the mean sky area value drops from ~10^4 to ~200 deg^2. From 45 Mpc onward, the betterment of the mean sky area value is not as meaningful, reaching ~80 deg^2 when Virgo has a BNS range of 100 Mpc. In the P_{min} case, the distribution of the mean sky area values is quasilinear, progressing continuously from ~2×10^4 to 400 deg^2 for 0 and 100 Mpc, respectively.
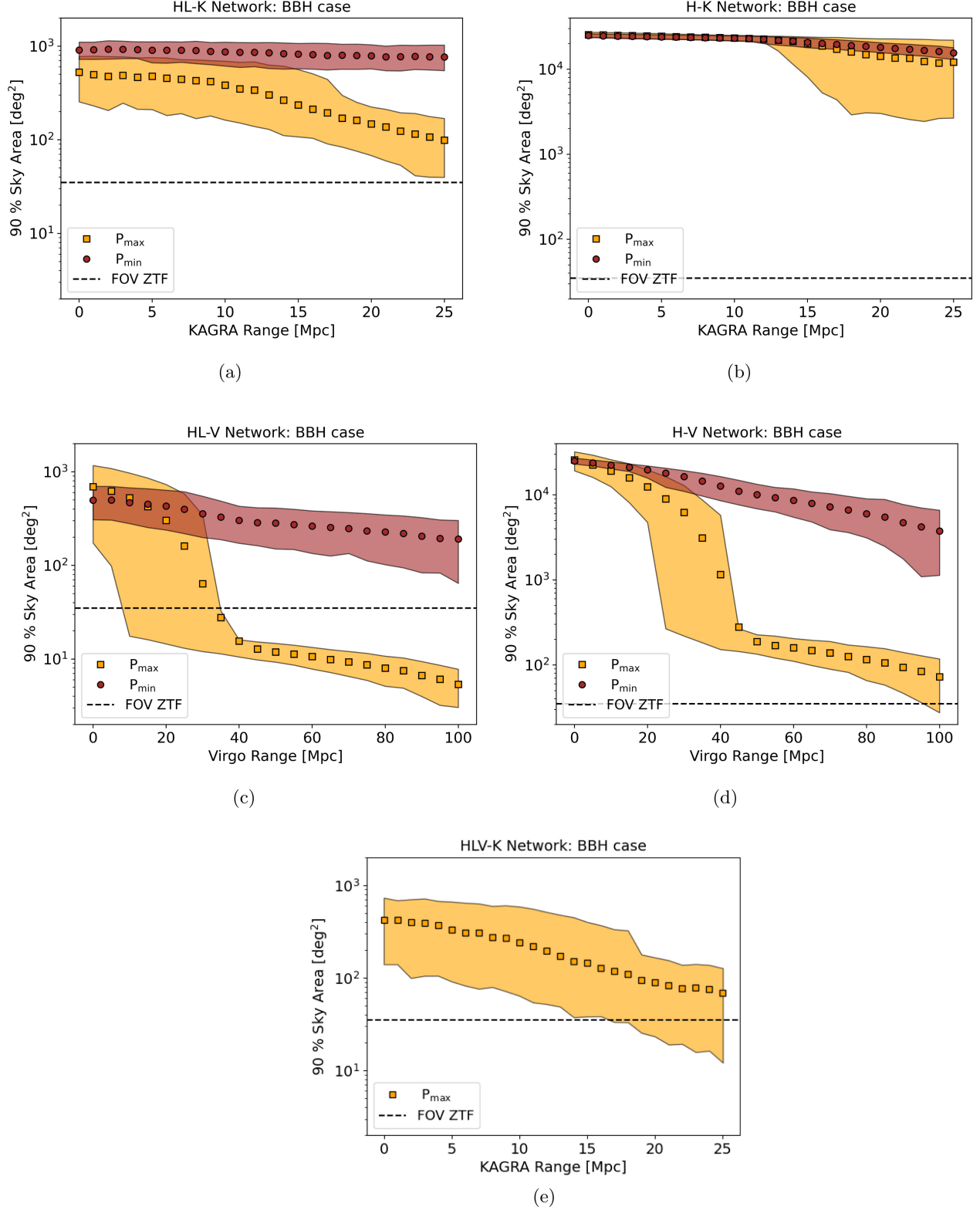
FIG. 4. Zero-spin binary black hole simulations. The mean and the 90% probability contour of the sky area for varying detector BNS range values for a gravitational-wave signal emitted by a BBH coalescence from the P_{max} and P_{min} source location for the least sensitive detector, orange and brown points and areas, respectively. The points, brown dots, and orange squares represent the mean value, and the areas stretch from the 5% to the 95% quantiles for each BNS range bin. The black dotted line corresponds to the field of view (FOV) of the Zwicky Transient Facility (ZTF). We obtained the 0 Mpc points from simulations excluding the least sensitive detector. We fixed the BNS range of the two LIGO detectors at 180 Mpc. (a) Varying the KAGRA detector and employing the LHK network. (b) Varying the KAGRA detector and employing the HK network. (c) Varying the Virgo detector and employing the LHV network. (d) Varying the Virgo detector and employing the HV network. (e) Varying the KAGRA detector and employing the LHVK network. Virgo's BNS range is fixed at 30 Mpc.

Finally, Fig. 4(e) shows the mean sky area values and 90% probability contours obtained with the methods outlined in Sec. II A from simulated detections of BBH merger signals with the HLV-K detector network when varying the BNS range of the KAGRA detector only. We fix the BNS range of the Virgo detector at 30 Mpc and employ the P_{max} source location for the KAGRA detector in all the runs. We observe a continuous improvement of the sky area from 5 to 25 Mpc, with the mean value passing from $\sim$500 to $\sim$100 deg^2. This suggests that, even in a four-detector network, adding an interferometer up to 10 times less sensitive than the others but at a different spatial location and with a different relative orientation leads to a 75% reduction in the mean sky-localization area inferred with the network.

IV. RESULTS OF BINARY NEUTRON STAR SIMULATIONS

We simulate gravitational-wave signals from nonspinning BNS mergers following the same procedure of Sec. III. The BNSs are placed at a distance from Earth of 100 Mpc and have a chirp mass of $1.198 M_\odot$, comparable to the first BNS merger event GW170817 [112]. The complete list of parameter values can be found in the second column of Table II in Appendix A. For the gravitational-wave signal simulation and parameter estimation, we use the IMRPhenomPv2 [113] waveform approximant, and to speed up the evaluation of the likelihood function, we employ the reduced order quadrature basis from the analysis of GW170817 [114]. We list the priors in the second column of Table III. The results are presented in Fig. 5.

In Fig. 5(a), we show the mean and the 90% quantile region of the sky-localization area as a function of the BNS range of the KAGRA detector for the P_{max} and P_{min} source locations for KAGRA. We use the same color scheme as in Sec. III. The points and regions have been obtained with the methods detailed in Sec. II A from the parameter estimation results of simulated gravitational-wave signals emitted by the coalescence of binary neutron star mergers using the HL-K detector network. The 0 Mpc point corresponds to the sky area obtained from an HL detector network run with identical source locations and parameters. While in the P_{min} source location case, there is no improvement in the mean sky area value from 0 to 25 Mpc, in the P_{max} case, the value decreases continuously from $\sim$200 to $\sim$30 deg^2 for the same range values.

Figure 5(b) shows the sky area results for the P_{max} and P_{min} source locations for the H-K detector network, varying BNS range of KAGRA. For the P_{max} case, the sky area improves from $\sim$15 Mpc onward, with the 90% quantiles spanning to 1 order of magnitude lower values than in the P_{min} case. The mean sky area values for the P_{max} case are of the order 1.2×10^4 deg^2, with KAGRA having a BNS range of 25 Mpc, compared to 1.5×10^4 deg^2 for the P_{min}

case. This trend is coherent with the corresponding binary black hole case shown in Fig. 4(b).

Figure 5(c) shows the mean sky area values and the 90% probability areas obtained from the parameter estimation runs using the HL-V detector network placing the source in the P_{max} and P_{min} source locations for Virgo. As in Fig. 4(c), we see that, for the P_{min} source location, the sky area values do not improve when Virgo's BNS range is wider, while in the P_{max} case, there is an improvement starting from 15 Mpc. This improvement is significant up to $\sim$40 Mpc, going from $\sim$200 deg^2 without Virgo to $\sim$4 deg^2 when Virgo has a BNS range of 40 Mpc. The sky area values remain roughly constant from 40 to 100 Mpc for this optimal case. In the P_{min} case, the sky area does not change between 0 and 40 Mpc and decreases minimally from 40 Mpc onward.

As for the BBH case, the sky area for the two-detector network, H-V, exhibits a similar evolution for the BNS range of Virgo. These results are visible in Fig. 5(d). In the optimal case, we see a considerable refinement of the sky area between 25 and 40 Mpc, with the mean value passing from 10^4 to 10^2 deg^2. This value continues to improve continuously up to 30 deg^2 at 100 Mpc. Also in the P_{min} case, different from the correspondent three-detector network results in Fig. 5(c), we see a noticeable improvement with increasing BNS range. Indeed, the mean sky area value is reduced to 3×10^3 deg^2 at 100 Mpc, with the 90% area reaching down to 400 deg^2, from 2.5×10^4 at 0 Mpc.

Finally, Fig. 5(e) is the correspondent of Fig. 4(e) for simulated detections of BNS merger signals with the HLV-K detector network when varying the BNS range of the KAGRA detector only. The network setup in the simulations is identical to the binary black hole case. Similarly, we observe a continuous improvement of the sky area, with the mean value decreasing from $\sim$100 to $\sim$30 deg^2. The 90% quantile region follows a similar trend, with the lower end going from $\sim$40 deg^2 without KAGRA to $\sim$5 deg^2 when KAGRA reaches a BNS range of 25 Mpc.

V. RESULTS OF HIGHLY SPINNING BINARY BLACK HOLES

Finally, we simulate gravitational-wave signals from highly spinning aligned BBHs employing the Hanford-Livingston-Virgo detector network and perform parameter estimation varying the BNS range of the Virgo detector only. In contrast to the previous subsection, we aim to understand how the BNS range of the Virgo detector impacts the inference of the intrinsic properties of the source. We focus on a high-spin BBH merger as the spin-related parameters, e.g., the effective spin and the individual spin magnitudes, are only broadly constrained by current detector network configurations, while they encode a large amount of information. Tighter constraints on these variables could lead to an enhanced understanding of the Universe's black hole population properties and their formation channels [115].
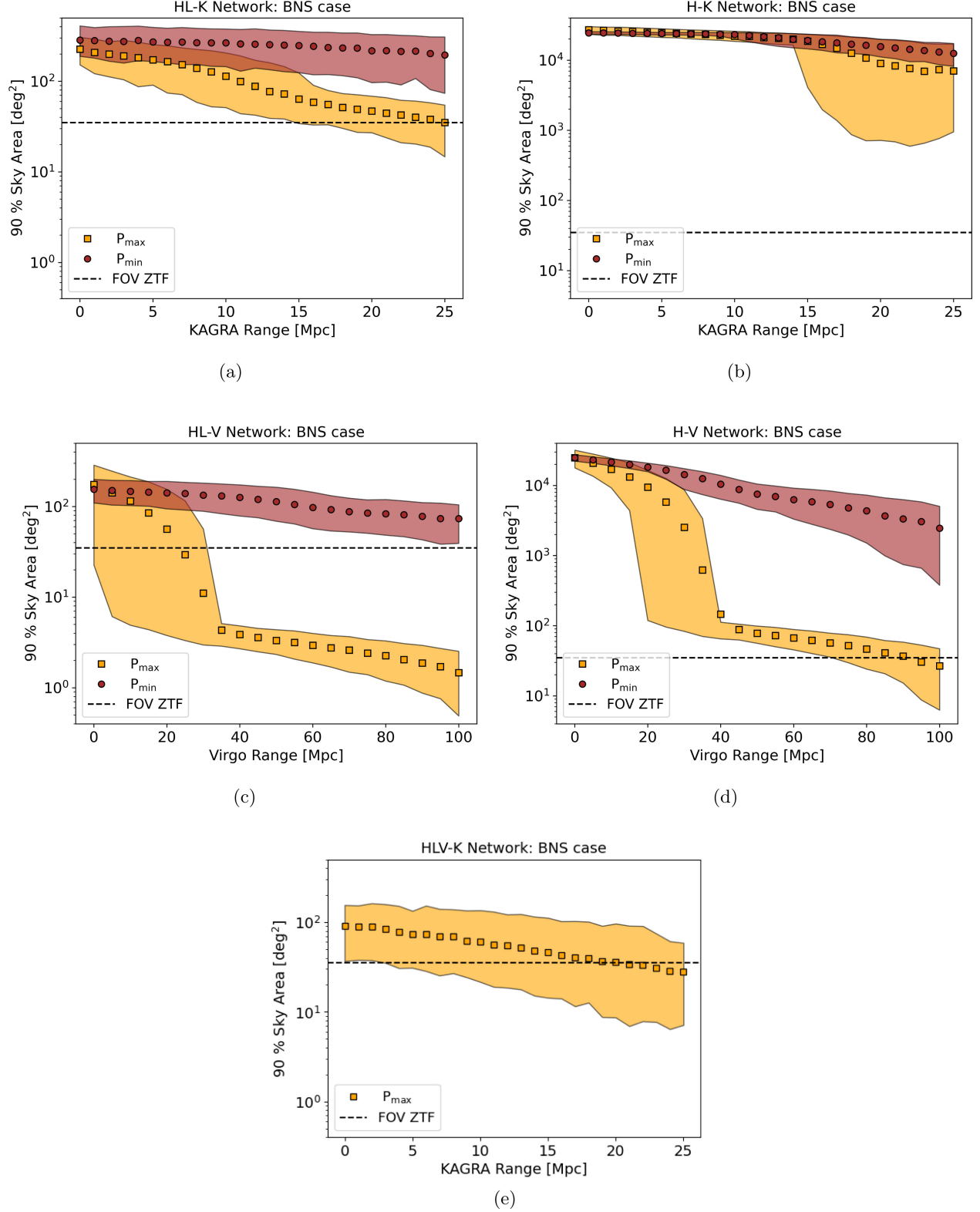
FIG. 5. BNS simulations. The mean and the 90% probability contour of the sky area for varying detector BNS range values for a gravitational-wave signal emitted by a BNS coalescence from the P_{max} and P_{min} source location for the least sensitive detector, brown and orange dots, and areas, respectively. The dots represent the mean value, and the areas stretch from the 5% to the 95% quantiles for each BNS range bin. The black dotted line corresponds to the field of view of the Zwicky Transient Facility. We obtained the 0 Mpc points from simulations excluding the least sensitive detector. We fixed the BNS range of the two LIGO detectors at 180 Mpc. (a) Varying the KAGRA detector and employing the LHK network. (b) Varying the KAGRA detector and employing the HK network. (c) Comparing the Virgo detector and employing the LHV network. (d) Varying the Virgo detector and employing the HV network. (e) Varying the KAGRA detector and employing the LHVK network. Virgo's BNS range is fixed at 30 Mpc.

We simulate a signal with the following arbitrary choice of parameters: we employ a chirp mass of $27.93M_\odot$ and a χ_{eff} value of 0.91 and assume that the spins are aligned so that $\chi_p = 0$ and the tilt angles are null. The effective spin is a dimensionless parameter quantifying the alignment of the spins of the binary components given by

$$\chi_{\text{eff}} = \frac{(m_1 \cdot \chi_1 + m_2 \cdot \chi_2) \cdot \hat{L}}{M}, \qquad (4)$$

with $m_{1/2}$ denoting the masses of the two black holes, M their total mass, L their angular momentum, and $\chi_{1/2}$ the individual dimensionless spins. The parameter χ_p, introduced in Schmidt *et al.* [116], combines the spin magnitudes and their relative orientation to the total angular momentum, effectively characterizing the degree of precession in a BBH system. The complete list of values is reported in the third column of Table II in Appendix A, while the priors used for the runs are listed in the third column of Table III. For the sky localization we choose the P_{max} position for Virgo, as we want to investigate the effect this detector has on the network. We also adjust the settings for the DYNESTY sampler, as visible in Table IV in Appendix A, to reduce the bias in the posterior probability results.

The analysis of these simulations takes significant computational effort. To alleviate this, we will apply a rejection sampling approach using a base analysis as a proposal distribution and reweighting for each rescaled Virgo BNS range value. Specifically, we begin with a single posterior obtained for the HLV network when Virgo has a BNS range of 50 Mpc applying the standard nested sampling algorithm as described in Sec. II. We choose 50 Mpc, as this is above the point where the extrinsic parameters are well constrained by triangulation. This initial HLV analysis takes ≈ 8 h using 30 CPU cores. Each reweighting takes ≈ 10 min on a single CPU core. This vast improvement is only possible because, as we increase the BNS range of Virgo, the posterior narrows marginally such that the base analysis is an excellent generating distribution.

After performing the base analysis and obtaining a set of posterior samples $\{\theta_i\}$ for a single noise realization, we obtain the weight for the ith sample as

$$W_i = \frac{f(\theta_i)}{Mg(\theta_i)}, \quad \text{with} \quad f(\theta_i) \le M \times g(\theta_i), \qquad (5)$$

where $g(\theta_i)$ is the generating distribution, $f(\theta_i)$ is the resampling distribution, and M is a factor used to ensure that the generating distribution encompasses the resampling distribution, effectively normalizing the weights to the range [0, 1]. In our case, the generating distribution is $g(\theta_i) = \mathcal{L}(\theta_i|H_{180})\mathcal{L}(\theta_i|L_{180})\mathcal{L}(\theta_i|V_{50})\pi(\theta_i)$, while the resampling distribution is $f(\theta_i) = \mathcal{L}(\theta_i|H_{180})\mathcal{L}(\theta_i|L_{180})\mathcal{L}(\theta_i|V_j)\pi(\theta_i)$

where the subscripts for the detectors indicate the BNS range, expressed in Mpc, of the PSDs used for the evaluation of the noise realizations and j ranges from 60 to 180 Mpc. Therefore, since the likelihood for the Hanford and Livingston data is identical, we can simplify the weights from Eq. (5) to be

$$W_i = \frac{\mathcal{L}(\theta_i|V_j)}{M\mathcal{L}(\theta_i|V_{50})}. \qquad (6)$$

The basic idea of rejection sampling is to draw random samples from the generating distribution g, calculate the related weights, and compare these to a random number taken from a uniform distribution between 0 and 1 [117]. If the weight is bigger than the random number, we accept the sample and include it in the posterior; otherwise, we discard it. It is important to carefully choose the value of M so that it satisfies the condition in Eq. (5) and at the same time does not make the sampling inefficient by being too large. We choose the value of M by calculating

$$\log(M) = \text{Max}_i \left(\frac{\log(\mathcal{L}(\theta_i|V_j))}{\log(\mathcal{L}(\theta_i|V_{50}))} \right) + 0.1, \qquad (7)$$

over set of samples.

To account for the high variability of the individual noise realizations, for each BNS range value we perform 20 iterations of the resampling routine. We focus on the BNS range between 50 and 180 Mpc and employ PSDs obtained with the methods described in Sec. II progressively increasing the BNS range by tens. We then combine the samples from the multiple iterations before postprocessing the data.

In Fig. 6 we show a summary of our results. In each of the panels, we show the mean, blue dots, and 90% probability contours, red lines, of the selected parameter versus the different BNS ranges of the Virgo detector. The 90% contour is centered around the mean for all variables except for χ_p. To account for the latter's true value corresponding to the boundary of the parameter's lower constraint, its 90% contour is taken from the lower boundary to the 90% quantile. The true values used for the simulation of the gravitational-wave signal correspond to the black dotted horizontal lines. Overall, we notice a consistent improvement in the mean value and a tightening of the 90% probability contours when increasing Virgo's BNS range. This trend is particularly evident in Figs. 6(a) and 6(c), depicting the results for the detector-frame chirp mass and the effective spin parameter. For both the chirp mass and effective spin, the mean value gets continuously closer to the true value reaching a 60% and 45% improvement at 180 Mpc, respectively. At the same time, the 90% probability contours decrease by 30% for both parameters from 60 to 180 Mpc. The mass ratio shown in Fig. 6(b) shows a similar trend going from 60 to 180 Mpc, with a
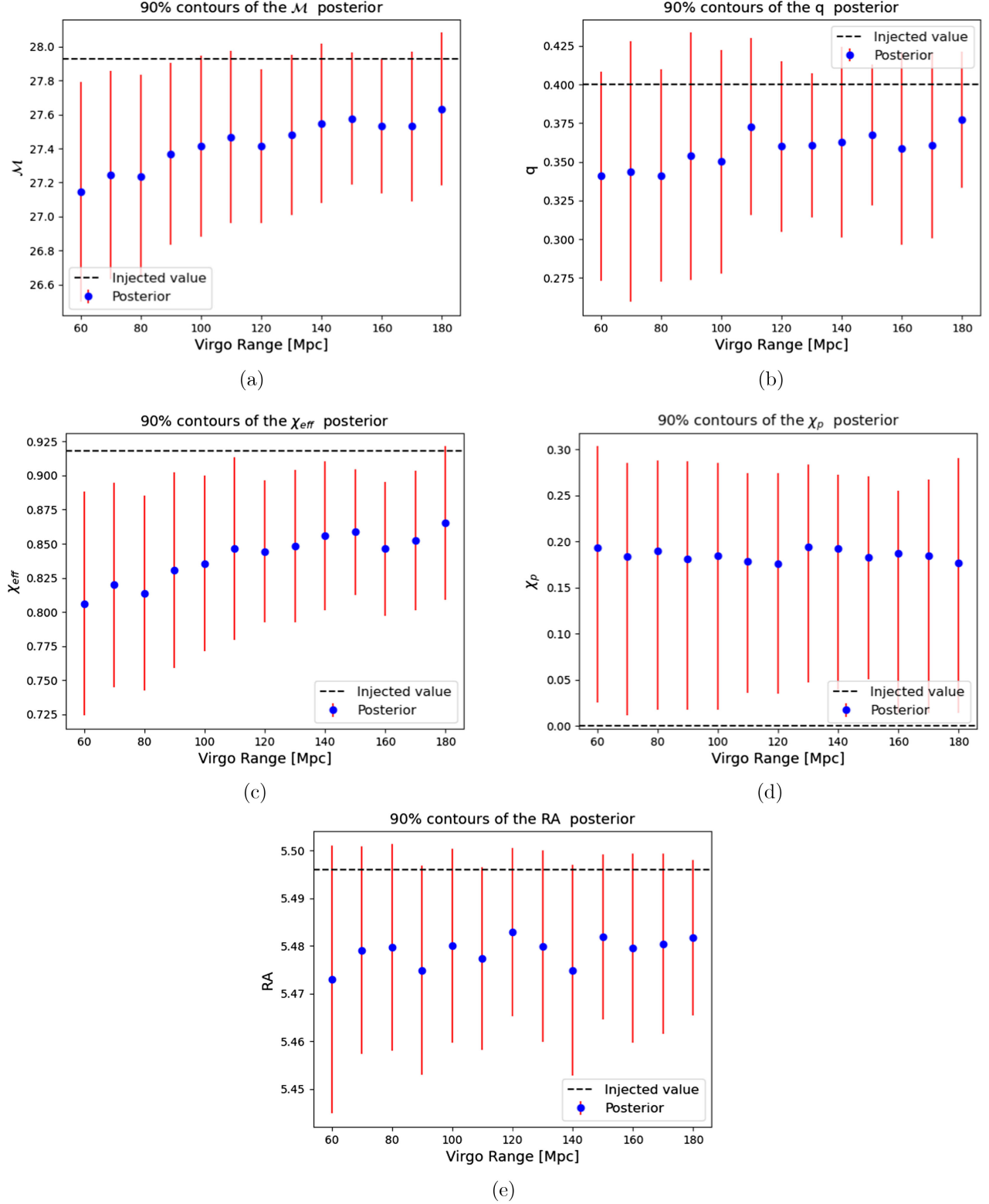
FIG. 6. High-spin binary black hole simulations. (a) The mean, blue dots, and 90% posterior probability contour, red line, of the detector-frame chirp mass obtained varying the BNS range of Virgo in the parameter estimation analysis of a simulated high-spin binary black hole merger signal. We employ the HL-V detector network, fixing the BNS range, noise realization, and detector response of the two LIGO detectors. The black dotted line represents the true chirp mass value of the simulated signal. (b) The same quantities as in (a) for the mass ratio. (c) The same quantities as in (a) for the effective spin parameter χ_{eff}. (d) The same quantities as in (a) for the spin precession parameter χ_p. (e) The same quantities as in (a) for the right ascension.

60% improvement in the mean value and a 30% decrease in the 90% probability contour. We notice that, in this case, the most significant betterments happen at sensitivities above 100 Mpc. Finally, in Figs. 6(d) and 6(e) we report the results for χ_p and the right ascension, respectively. As we are analyzing a nonprecessing binary system, we expectedly recover χ_p to be consistent with zero at all sensitivities. For the right ascension, we obtain only minor improvements passing from 60 to 180 Mpc. This is not surprising because, as noted in Sec. III, the sky localization shows the largest improvements at sensitivities between 20 and 40 Mpc. Overall, we can conclude that when Virgo reaches sensitivities starting from approximately half of the LIGO sensitivities, i.e., 90/100 Mpc, the inference of the intrinsic source parameters improves significantly.

VI. MINIMUM-FREQUENCY STUDY

Gravitational-wave signals from merging black holes and neutron stars sweep up in frequency during the inspiral stage before their eventual merger and ringdown. From a simple post-Newtonian calculation, it can be shown (see, e.g., Peters and Mathews [118]) that the time to merger from a frequency f_0 is

$$t_m = 1.5 \text{ s} \left(\frac{20 M_\odot}{\mathcal{M}}\right)^{5/3} \left(\frac{20 \text{ Hz}}{f_0}\right)^{8/3}, \qquad (8)$$

where $\mathcal{M}$ is the detector-frame chirp mass defined in Eq. (3). The power of 8/3 means that signals spend far longer at lower frequencies than at the higher frequencies near the merger (this expression breaks down near the merger itself but is a good approximation for the early inspiral). However, the noise curve of the detector steeply rises at low frequencies. As such, analyses often assume a minimum frequency $f_{\min}$ below which the signal has negligible contributions to the signal-to-noise ratio (SNR). However if $f_{\min}$ is chosen to be too large, the SNR will be reduced, leading to an increase in the associated uncertainty of the source parameters. For example, Villa-Ortega *et al.* [119] find that the uncertainty on the distance scales with the network SNR[1] raised to the power -0.322 and we similarly expect all parameters to scale inversely with the network SNR. Our goal in this section is to investigate the appropriate choice of $f_{\min}$ for advanced-era detectors. To do this, we will construct a metric to predict the proper minimum frequency.

We begin with the definition of $f_{\min}$: in standard approaches to Bayesian inference for signals, we assume a stationary Gaussian noise resulting in a log-likelihood

---

[1]The network SNR is the square root of the quadrature sum of per-detector SNRs.

$$\log \mathcal{L}(d|\theta) \propto \sum_k \frac{2|\tilde{d}_k - \tilde{\mu}_k(\theta)|^2}{T S_k}, \qquad (9)$$

where T is the data duration, k is the index of the frequency bin, $\tilde{d}$ is the complex frequency-domain data, $\tilde{\mu}(\theta)$ is the frequency-domain source model evaluated at a set of source parameters θ, and S is the PSD (see, e.g., Finn [120] and Veitch *et al.* [121]). In practice, the minimum frequency is implemented by neglecting to sum components below $k_{\min}$, the frequency bin associated with $f_{\min}$.

The introduction of $f_{\min}$ then informs the choice of T, the duration of data to analyze. Choosing T to be much larger than the actual signal duration is inefficient, requiring unnecessary computation and ultimately increasing the computational cost of an analysis. The standard in the field remains to take $f_{\min} = 20$ Hz and then choose T to be the next power of 2 greater than the estimated time to merger [either using Eq. (8) or an improved model incorporating other physical effects].

This standard has been in place since the first detection [122], though with some exceptions. It is common to increase $f_{\min}$ as a mechanism to mitigate non-Gaussianity in the detector [123]. However, it has also been decreased to maximize the number of cycles in band for analysis (see, e.g., Abbott *et al.* [124] and Abbott *et al.* [74] which used a minimum frequency of 19.4 and 11 Hz, respectively).

While the 20 Hz rule of thumb is built on a solid understanding of the detector performance over the first observing runs, recent upgrades have seen improvements in the low-frequency sensitivity and future detector developments aim to improve performance further. This leads us to ask: what conditions should be met for $f_{\min}$ to be decreased? Our ultimate goal is to develop a simple-to-compute metric that can provide gravitational-wave astronomers with a better-informed rule of thumb for choosing $f_{\min}$.

To construct our metric, we use the matched-filter SNR

$$\rho_{\mathrm{mf}} = \frac{\langle \tilde{d}, \tilde{\mu}(\theta) \rangle}{\sqrt{\langle \tilde{\mu}, \tilde{\mu}(\theta) \rangle}}, \qquad (10)$$

where $\langle a, b \rangle$ denotes the noise-weighted inner product

$$\langle a, b \rangle = \frac{4}{T} \sum_{k=k_{\min}}^{k_{\max}} \Re\left(\frac{a_k b_k^*}{S_k}\right), \qquad (11)$$

and $k_{\min}$ corresponds to the minimum-frequency bin $f_{\min}$, while $k_{\max}$ corresponds the maximum-frequency bin (which we set to 2048 Hz).

Taking time-domain data from a given detector, we Fourier transform to the frequency domain and add to it a simulated fiducial signal; we then use that same signal to

calculate the matched-filter SNR. That is, the simulated signal added to the data is also used in Eq. (10).

Finally, we vary $f_{\min}$ and define $\hat{f}_{\min}$ to be the minimum frequency at which $\rho_{\rm mf}$ decreases by $\epsilon = 0.1\%$ relative to the value as calculated at $f_{\min} = 15$ Hz (an arbitrary choice considered to be sufficiently low to represent the maximum SNR). Within this definition, there are two tuning parameters. First, the choice of fiducial signal. We apply two choices: a fiducial BBH and a fiducial BNS. For both signals, we use the IMRPhenomXAS waveform model [105] with zero spin, equal masses, and arbitrary choices of $\theta_{\rm JN} = 0.4$, $\psi = 2.659$, $\phi = 1.3$, $\alpha = 1.375$, and $\delta = -1.2108$ for the inclination angle, polarization angle, phase, right ascension, and declination. The two differ only in the choice of chirp mass and luminosity distance for which we use $30 M_\odot$ and 500 Mpc for the BBH case and $2 M_\odot$ and 50 Mpc for the BNS case. The second tuning parameter is ϵ, which sets the threshold loss of SNR. Choosing ϵ to be arbitrarily small simply recovers the minimum allowed frequency, i.e., 15 Hz. We choose 0.1% as a conservative estimate, being sufficiently small such that we would not expect any meaningful changes to the inferred parameter estimates. Finally, we note that this definition has close parallels with the development of varying minimum-frequency bounds in the construction of search template banks [125].

To investigate how the choice of minimum frequency impacts measurements of the source parameters, we begin by calculating the minimum frequency for realizations of the noise drawn from the PSDs studied in Sec. II. Generating multiple realizations of the noise at different sensitivities of the Virgo detector and the fixed LIGO O4 high sensitivity, in Fig. 7 we plot the mean values along with the 90% interval and a color map indicating the mean SNR. We do this for both a fractional SNR loss of $\epsilon = 0.1\%$ and 1%. The figure demonstrates that, for LIGO and Virgo at a BNS range of 180 Mpc, the suggested minimum frequency is between 18 and 20 Hz (for a loss of 0.1%) and 24 and 26 Hz (for a loss of 1%). The Virgo mean for 0.1% loss is marginally lower than LIGO (though within the uncertainty interval); this is likely due to the higher sensitivity of the Virgo design PSD at low frequencies, i.e., 10–20 Hz [126]. The inverse is true for the 1% loss mean minimum frequency. This agrees with the trend of the PSDs in Fig. 1, as the LIGO PSD falls underneath the Virgo one from $\simeq$20 Hz onward. As we decrease the sensitivity of the Virgo detector, the trend indicates that the suggested minimum frequency should also decrease. However, we note that the SNR is also decreasing. This results from using the fractional loss of SNR as our criteria, while reducing the minimum frequency induces an absolute loss of SNR: for higher sensitivities where the SNR is larger, the gain achieved from decreasing the frequency is relatively small compared to when the detector sensitivity is smaller with a similarly smaller SNR. Finally, while for both LIGO
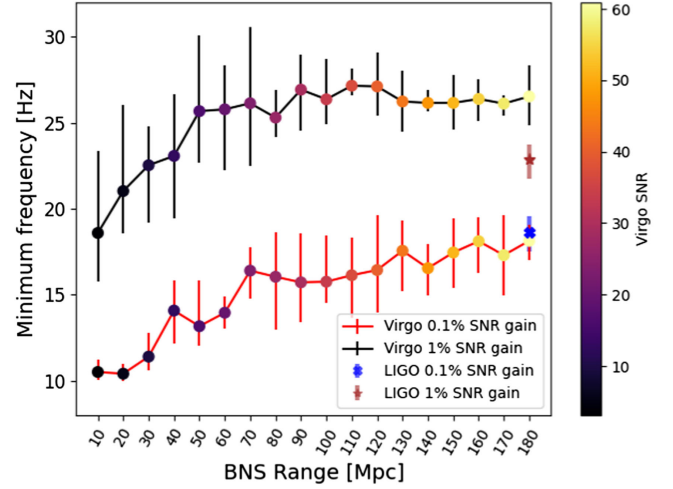

FIG. 7. The estimated mean minimum frequency (calculated at a fractional SNR loss of $\epsilon = 0.1\%$ and 1%) using data generated from the scaled PSDs for O4 and O5 sensitivities of the Virgo (red and black) and LIGO (blue and brown) detectors. We compute the average and uncertainty interval over six noise realizations and vary the BNS range for Virgo from 10 to 180 Mpc. All simulated signals utilize the fiducial BBH simulated signal. The color map shows the mean of the SNR ratio for Virgo, while for the fixed LIGO detector the average SNR is 61.4 and 60.8, blue and brown, respectively.

and Virgo at their advanced-era configuration we predict a suggested minimum frequency below 20 Hz, we note that this is using a relative loss of just 0.1% where negligible changes to the SNR are expected. Meanwhile, for a loss of 1%, the minimum frequencies are all above the nominal 20 Hz minimum frequency used in practice.

To study the behavior of the minimum-frequency criteria in real data, we apply our metric to observational data from the third observing run (O3) of the LIGO-Virgo detector network. In Fig. 8, we plot the estimated value of $\hat{f}_{\min}$ in a sliding window for the three detectors using data from the Gravitational Wave Open Science Center [127]. We do this first for the fiducial BBH (left panel) and then for the fiducial BNS (right panel). The estimates are time averaged by the sliding window, smoothing out variations on short timescales (e.g., due to the relative sensitivity to the fiducial signal as a function of the rotation of Earth). Comparing the detectors, we see that, in the BBH case, the average for the Hanford instrument is robustly over the 20 Hz standard, while for Livingston, it averages around 19 Hz. This indicates that there may be some minor improvements possible for O3 analyses that use a minimum frequency of 20 Hz and include data from Livingston. However, we reiterate that our metric is highly conservative (we lose 0.1% of the SNR for a perfectly correlated template), and we do not expect the improvements to be significant. Meanwhile, Virgo has the lowest values of $\hat{f}_{\min}$ of the three. While, in principle, this suggests that using a smaller value of $f_{\min}$ could also improve analyses, one should also
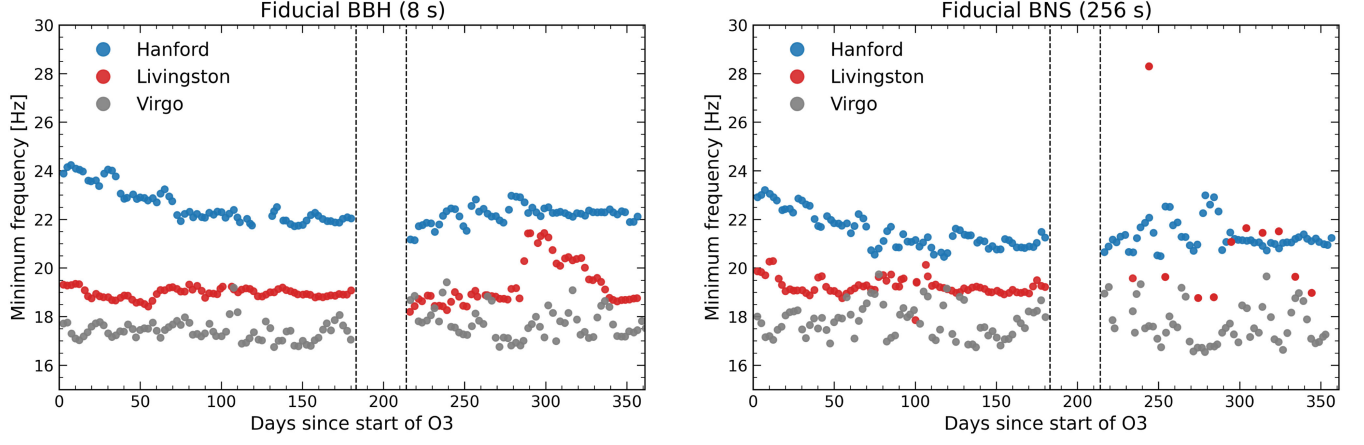
FIG. 8. The estimated mean minimum frequency and 90% interval for LIGO Hanford (H1), LIGO Livingston (L1), and Virgo (V1) over the third observing run for the fiducial BBH (left) and fiducial BNS (right). To estimate the mean and interval, we apply a half-overlapping sliding window with a duration of 5 days. Dashed vertical lines mark the beginning and end of the A/B data collection periods.

factor in the relative SNR between detectors. For the fiducial BBH, Hanford and Livingston have a median SNR of approximately 30, while Virgo has a median SNR of 13; for the fiducial BNS, the SNRs are approximately 40 for Hanford and Livingston, but 20 for Virgo. Since the network SNR will be dominated by the more sensitive detectors, for most observations, we expect the standard 20 Hz minimum frequency to be more than sufficient.

We have introduced $\hat{f}_{\min}$ as a diagnostic tool to predict when analysts may wish to consider using a minimum frequency. We note that our choices of tuning parameter mean that $\hat{f}_{\min}$ should not be considered an absolute prediction. For specific analyses, we suggest performance studies be performed to ensure their choice of $f_{\min}$ is robust. However, we also note that $\hat{f}_{\min}$ offers a useful heuristic to understand the relative performance of the detector: it, therefore, may be useful in future observing runs as an online monitor or to understand the impact of specific detector improvements.

VII. DISCUSSION

We have simulated gravitational-wave signals from compact binary mergers to study the impact of the addition of Virgo and KAGRA on the ground-based detector network. We have focused on analyzing the improvements in the sky-localization constraints for zero-spin binary black holes and neutron star binaries and on the intrinsic source-parameter estimates for high-spin aligned binary black holes. In Secs. III and IV, we have shown the results of the evolution of the sky-localization area for different detector networks when varying the BNS range of their least sensitive detector. Our results confirm that the addition of the Virgo and KAGRA detectors to the network comprising the two LIGO interferometers would improve the sky-localization capabilities even when these additional

detectors are not at their design sensitivity. Our findings expand on the results from several previous studies [20,45,49] that have focused on networks of equally sensitive detectors. Looking at the current sensitivities of ground-based interferometers, we find that the inclusion of Virgo into an HLV network is most beneficial starting from a Virgo BNS range of around 30–50 Mpc, corresponding to ~1/5 of the BNS range of the LIGO detectors, that we fixed at 180 Mpc. These results, which depend on the specific position of the source relative to the Virgo detector and its inclination, are consistent with the relative BNS range values of ≃1/5–1/6 that we computed in Sec. II. We find that our results also agree with the analysis of the binary black hole merger signal GW170814 [32]. For this first clear three-detector observation, the 90% sky-localization area improves from 1160 to 60 deg^2 when adding the Virgo detector data, whose BNS range at the time was roughly 1/3 of the LIGO detector's BNS range. Although the source of GW170814 was much nearer than our simulated one, this is comparable to the improvement we see in Fig. 4(c) for 60 Mpc, i.e., 10 deg^2 compared to the 800 deg^2 of the HL network.

A more general heuristic consideration is to look at the cumulative distribution of the antenna pattern function of the two individual LIGO detectors. When these are marginalized over all four angular parameters, one can notice that Virgo is almost exactly orthogonal to the LIGO detectors, as seen in Fig. 3. So, it would have the same BNS range as LIGO, or better, for about half of all the sources even if its BNS range was a factor of 2 smaller. Since we can argue that it would be enough to observe sources at about 1/3 of the LIGO signal-to-noise ratio in Virgo to still have meaningful parameter estimation, then Virgo would need to have at least a BNS range a sixth that of LIGO, or ≃30 Mpc average for about half of the sources. Comparing the field of view values of current optical telescopes,

presented in Sec. I, with the results of our simulations, we notice that the Virgo detector would allow for an easier follow-up from 30 and 90 Mpc onward, for the HLV and HV detector networks, respectively, for a BNS signal. In the nonspinning binary black hole case, the sky-localization area is reduced to $\sim$10 deg^2 when Virgo is added to the HLV network with a BNS range above 45 Mpc. For all the other two- and three-detector networks, despite the significant improvements in the localization constraints, these do never fall below the 10 deg^2 threshold. It is still noteworthy that the addition of KAGRA, with a BNS range of 25 Mpc, into the HLK network reduces the inferred sky area from 200 to 35 deg^2 for a binary neutron star source. To test if a similar drop in the 90% sky area would be achieved when KAGRA reaches a BNS range 1/5–1/6 that of the LIGO detectors, for Fig. 11 in Appendix B we extended Fig. 5(a) to BNS range values up to 50 Mpc. We do not recover the same trend of the Virgo detector. This can be explained by the better sensitivity of Virgo at low frequencies which complements the LIGO detectors' sensitivity, while KAGRA does have a lower low-frequency sensitivity. From our four-detector network results, shown in Figs. 4(e) and 5(e), we see that when Virgo has a BNS range of 30 Mpc, 1/6 of LIGO's, the addition of the KAGRA detector is still useful to constrain the sky area of events maximizing KAGRA's antenna pattern function. Specifically, for the binary neutron star case, the sky area can be constrained to under $\sim$35 deg^2 when KAGRA reaches a BNS range greater than 20 Mpc, corresponding to $\sim$1/9 of LIGO's. The mentioned results are obtained for a specific case, i.e., we consider a maximized Virgo antenna pattern function and a fixed distance, but our choice of parameters is a good approximation of the average values for the currently detectable population of sources [23]. In Figs. 9 and 10 in Appendix B, we show the same quantities as in Secs. III and IV obtained using P_{best} as the source location, recovering comparable results. Furthermore, our focus on the ratios of relative detector sensitivities in a network easily allows for a translation of our results to future detector networks.

In our analysis, we also focused on two-detector networks considering the variable duty factor the two LIGO detectors had in the previous observation runs, e.g., 65.3% and 61.8% during O2 for Hanford and Livingston, respectively [51]. We found that, even in the two-detector cases, the addition of Virgo and KAGRA can have an important impact on the performance of the network. With Virgo, at a BNS range of 100 Mpc or higher, we can expect the sky localization to be constrained to values smaller than the field view of current optical telescopes. This would highly increase our chances of detecting a multimessenger event.

VIII. CONCLUSION

We have run parameter estimation with Bilby on simulated gravitational-wave signals from zero-spin black hole and neutron star binaries looking at the sky-localization capability of different detector network configurations. We have focused on the improvements related to the addition of the Virgo and KAGRA detectors. We kept the BNS range of the LIGO detectors fixed at 180 Mpc and varied the BNS range of the additional detector. We found that the Virgo detector allows for the most significant improvements in the sky localization when it reaches a BNS range that is approximately 1/6 that of the LIGO detectors. We expect a similar result for KAGRA, but we restrict our study to values up to 1/7 that of LIGO. Furthermore, we found that, in the four-detector case, the addition of KAGRA would be beneficial at sensitivities above 1/10 that of the LIGO detectors, if Virgo is at 1/6 of the LIGO BNS range.

We also simulated gravitational waves from aligned high-spin binary black holes and analyzed the improvements in the inference of the intrinsic source parameters with the sensitivity of the Virgo detector. We found the most significant improvements in the accuracy at sensitivities of the Virgo detector above half that of the LIGO detectors. We have developed a tool to determine the optimal minimum frequency, defined as the lowest frequency for which the signal-to-noise ratio does increase by more than 0.1% with respect to higher cutoff frequency values. Testing this on O3 data by adding simulated gravitational-wave signals, we found that 20 Hz is a good choice for the lower frequency cutoff in the parameter estimation analysis.

Finally, we want to emphasize that, even if we have just applied a naive scaling of the spectral density, we have a good understanding of the noise budget of the detectors as a combination of power laws. In the future, we could use this knowledge to develop an interface to track the real-time changes in the PSD with the improvements in the detector. The parameters of interest would be the fitting constants for each power law in the PSD. This could allow us to overcome the imperfect scaling used in this work and would give us a deeper understanding of the connection between detector improvements and noise curves. It would also be interesting to perform a similar study including the future LIGO India detector, looking at sky-localization and parameter estimation improvements in two-, three-, four-, and five-detector networks.

APPENDIX A: TABLES OF SIMULATION PARAMETERS AND PRIOR DISTRIBUTIONS

TABLE II. Parameter values for simulated gravitational-wave signals corresponding to nonspinning BBH, BNS, and high-spin BBH mergers. Values are given for the chirp mass ($\mathcal{M}$), mass ratio (q), luminosity distance (D_L), dimensionless spins (a_1 and a_2), tilt angles (tilt$_1$ and tilt$_2$), phase angles (ϕ_{12} and ϕ_{jl}), angular parameter (θ_{jn}), polarization angle (ψ), and overall phase. These simulated values serve as the ground truth for the simulated signals.

Parameter	BBH	BNS	High-spin BBH
$\mathcal{M}$	50	1.198	27.93
q	1	1	0.40
D_L	2000	100	2000
a_1	0	0	0.91
a_2	0	0	0.94
Tilt$_1$	0	0	0
Tilt$_2$	0	0	0
ϕ_{12}	0	0	0
ϕ_{jl}	0	0	0
θ_{jn}	0.4	0.4	0.4
ψ	2.66	2.66	2.66
ϕ	1.3	1.3	1.3

TABLE III. Prior distributions employed in the parameter estimation of simulated gravitational-wave signals arising from high-spin and nonspinning BBH and BNS mergers. The symbol $\mathcal{U}$ denotes a uniform prior, and λ^2 represents a power law prior within the specified ranges. The table details the priors for chirp mass ($\mathcal{M}$), mass ratio (q), individual masses (M_1 and M_2), dimensionless spins (χ_1 and χ_2), tilt angles (tilt$_1$ and tilt$_2$), DEC, luminosity distance (D_L), RA, and various angle parameters.

Parameter	BBH	BNS	High-spin BBH
$\mathcal{M}$	$\mathcal{U}$ [25, 60]	$\mathcal{U}$ [1.19799, 1.19801]	$\mathcal{U}$ [15, 60]
q	$\mathcal{U}$ [0.125, 1]	$\mathcal{U}$ [0.125, 1]	$\mathcal{U}$ [0.125, 1]
M_1	[1, 100]	[1, 100]	[5, 100]
M_2	[1, 100]	[1, 100]	[5, 100]
χ_1	$\mathcal{U}$ [0, 0.99]	$\mathcal{U}$ [0, 0.05]	$\cdots$
χ_2	$\mathcal{U}$ [0, 0.99]	$\mathcal{U}$ [0, 0.05]	$\cdots$
a_1	$\cdots$	$\cdots$	$\mathcal{U}$ [0, 0.99]
a_2	$\cdots$	$\cdots$	$\mathcal{U}$ [0, 0.99]
Tilt$_1$	$\cdots$	$\cdots$	Sin
Tilt$_2$	$\cdots$	$\cdots$	Sin
ϕ_{12}	$\cdots$	$\cdots$	$\mathcal{U}$ [0, 2π]
ϕ_{jl}	$\cdots$	$\cdots$	$\mathcal{U}$ [0, 2π]
D_L	λ^2 [10, 10000]	λ^2 [10, 500]	$\mathcal{U}$ [100, 5000]
DEC	Cos	Cos	Cos
RA	$\mathcal{U}$ [0, 2π]	$\mathcal{U}$ [0, 2π]	$\mathcal{U}$ [0, 2π]
θ_{jn}	Sin	Sin	Sin
ψ	$\mathcal{U}$ [0, π]	$\mathcal{U}$ [0, π]	$\mathcal{U}$ [0, π]
ϕ	$\mathcal{U}$ [0, 2π]	$\mathcal{U}$ [0, 2π]	$\mathcal{U}$ [0, 2π]

TABLE IV. Setting employed for the DYNESTY sampler of Bilby for the parameter estimation of the simulated gravitational-wave signals.

DYNESTY	nlive	npool	Sample	naccept
Zero-spin BBH/BNS	1000	30	Acceptance walk	60
High-spin BBH	2000	30	Acceptance walk	60

APPENDIX B: FIGURES AND TABLE FOR THE BEST NETWORK SKY LOCALIZATION

TABLE V. Table of the RA, DEC, and the values of the single detector's antenna pattern amplitude for the source localization maximizing the combined antenna power pattern function, P_{best}, for each of the network configurations. The GPS time is fixed at 1379969683.0.

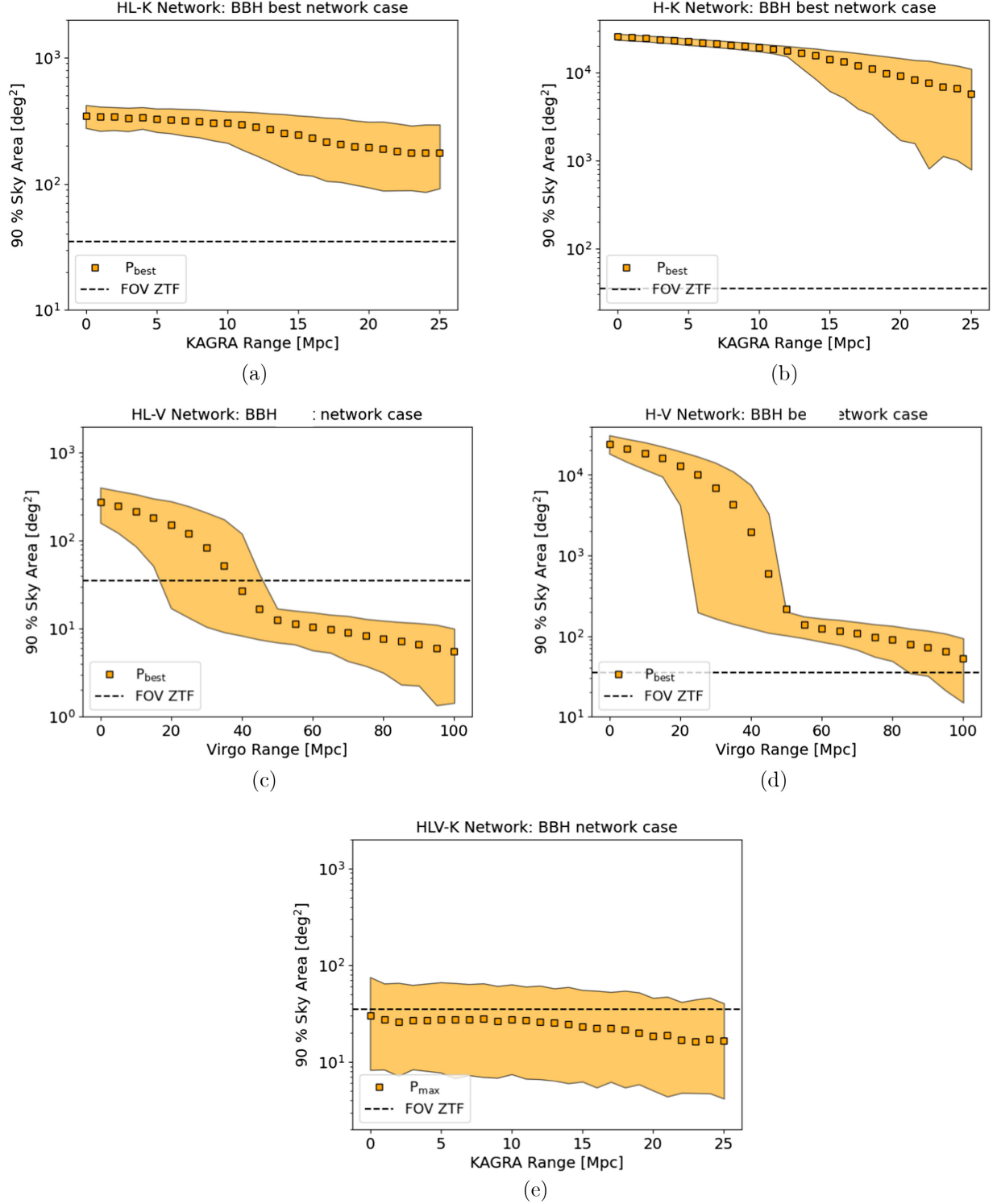|	RA (rad)	DEC (rad)	P_K	P_V	P_H	P_L
HK P_{best}	5.776	-0.952	0.62	0.17	0.72	0.32
HV P_{best}	5.311	0.917	0.10	0.88	0.35	0.34
HLK P_{best}	3.678	0.638	0.21	0.1	0.95	0.91
HLV P_{best}	4.008	0.690	0.10	0.23	0.87	0.98
HLVK P_{best}	3.873	0.529	0.20	0.20	0.85	0.98

FIG. 9. Zero-spin binary black hole simulations. The mean and the 90% probability contour of the sky area for varying detector BNS range values for a gravitational-wave signal emitted by a binary black hole coalescence from the P_{best} source location for each detector network, orange points and area, respectively. The orange squares represent the mean value, and the areas stretch from the 5% to the 95% quantiles for each BNS range bin. The black dotted line corresponds to the field of view of the Zwicky Transient Facility. We obtained the 0 Mpc points from simulations excluding the least sensitive detector. We fixed the BNS range of the two LIGO detectors at 180 Mpc. (a) Varying the KAGRA detector and employing the LHK network. (b) Varying the KAGRA detector and employing the HLK network. (c) Varying the Virgo detector and employing the LHV network. (d) Varying the Virgo detector and employing the HLV network. (e) Varying the KAGRA detector and employing the LHVK network. Virgo's BNS is fixed at 30 Mpc.
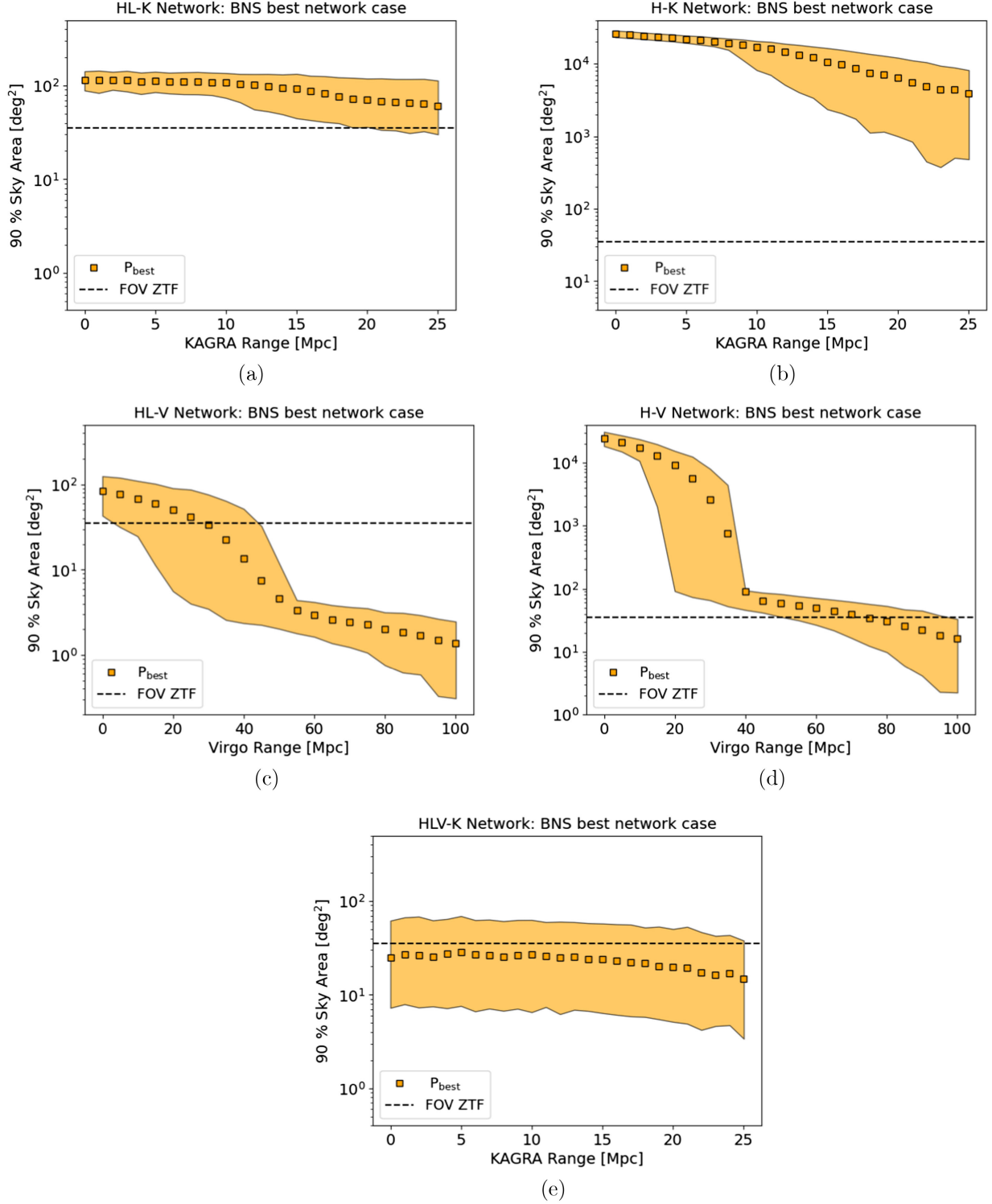
FIG. 10. Binary neutron star simulations. The mean and the 90% probability contour of the sky area for varying detector BNS range values for a gravitational-wave signal emitted by a binary neutron star coalescence from the P_{best} source location for each detector network, orange dots and areas, respectively. The squares represent the mean value, and the areas stretch from the 5% to the 95% quantiles for each BNS range bin. The black dotted line corresponds to the field of view of the Zwicky Transient Facility. We obtained the 0 Mpc points from simulations excluding the least sensitive detector. We fixed the BNS range of the two LIGO detectors at 180 Mpc. (a) Varying the KAGRA detector and employing the LHK network. (b) Varying the KAGRA detector and employing the HLK network. (c) Varying the Virgo detector and employing the LHV network. (d) Varying the Virgo detector and employing the HLV network. (e) Varying the KAGRA detector and employing the LHVK network. Virgo's BNS range is fixed at 30 Mpc.
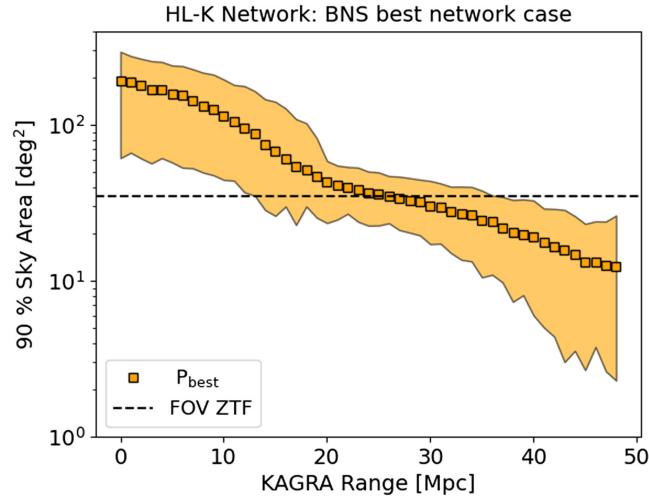
FIG. 11. Extension of Fig. 5(a) to higher binary neutron star range values. The mean and the 90% probability contour of the sky area for varying KAGRA BNS range values for a gravitational-wave signal emitted by a binary neutron star coalescence from the P_{max} for the HLK detector network, orange squares and areas, respectively. The squares represent the mean value, and the areas stretch from the 5% to the 95% quantiles for each BNS range bin. The black dotted line corresponds to the field of view of the Zwicky Transient Facility. We obtained the 0 Mpc points from simulations excluding the KAGRA detector. We fixed the BNS range of the two LIGO detectors at 180 Mpc.

[1] B. P. Abbott *et al.* (LIGO Scientific and Virgo Collaborations), Phys. Rev. Lett. **116**, 061102 (2016).

[2] B. P. Abbott *et al.* (LIGO Scientific and Virgo Collaborations), Phys. Rev. Lett. **119**, 161101 (2017).

[3] B. P. Abbott *et al.* (LIGO Scientific and Virgo Collaborations), Phys. Rev. D **100**, 104036 (2019).

[4] R. Abbott *et al.* (LIGO Scientific and Virgo Collaborations), Phys. Rev. D **103**, 122002 (2021).

[5] R. Abbott *et al.* (LIGO Scientific, Virgo, and KAGRA Collaborations), arXiv:2112.06861.

[6] B. P. Abbott *et al.* (LIGO Scientific and Virgo Collaborations), Phys. Rev. X **9**, 011001 (2019).

[7] B. Margalit and B. D. Metzger, Astrophys. J. Lett. **850**, L19 (2017).

[8] B. P. Abbott *et al.* (LIGO Scientific and Virgo Collaborations), Phys. Rev. Lett. **121**, 161101 (2018).

[9] R. Nair, S. Perkins, H. O. Silva, and N. Yunes, Phys. Rev. Lett. **123**, 191101 (2019).

[10] B. P. Abbott *et al.* (LIGO Scientific, Virgo, 1M2H, Dark Energy Camera GW-E, DES, DLT40, Las Cumbres Observatory, VINROUGE, and MASTER Collaborations), Nature (London) **551**, 85 (2017).

[11] J. Aasi *et al.* (LIGO Scientific Collaboration), Classical Quantum Gravity **32**, 074001 (2015).

[12] F. Acernese *et al.* (Virgo Collaboration), Classical Quantum Gravity **32**, 024001 (2015).

[13] T. Akutsu *et al.* (KAGRA Collaboration), Prog. Theor. Exp. Phys. **2021**, 05A101 (2021).

[14] B. P. Abbott *et al.* (LIGO Scientific and Virgo Collaborations), Phys. Rev. X **9**, 031040 (2019).

[15] R. Abbott *et al.* (LIGO Scientific and Virgo Collaborations), Phys. Rev. X **11**, 021053 (2021).

[16] The LIGO Scientific, the Virgo, and the KAGRA Collaborations *et al.*, arXiv:2111.03606.

[17] C. S. Unnikrishnan, Int. J. Mod. Phys. D **22**, 1341010 (2013).

[18] D. Reitze *et al.*, Bull. Am. Astron. Soc. **51**, 035 (2019).

[19] M. Punturo, M. Abernathy, F. Acernese, B. Allen, N. Andersson *et al.*, Classical Quantum Gravity **27**, 194002 (2010).

[20] B. F. Schutz, Classical Quantum Gravity **28**, 125023 (2011).

[21] B. P. Abbott *et al.* (LIGO Scientific and Virgo Collaborations), Astrophys. J. Lett. **882**, L24 (2019).

[22] R. Abbott *et al.* (LIGO Scientific and Virgo Collaborations), Astrophys. J. Lett. **913**, L7 (2021).

[23] R. Abbott *et al.* (KAGRA, Virgo, and LIGO Scientific Collaborations), Phys. Rev. X **13**, 011048 (2023).

[24] B. P. Abbott *et al.* (LIGO Scientific, Virgo, ASKAP, BOOTES, DES, Fermi GBM, Fermi-LAT, GRAWITA, INTEGRAL, iPTF, InterPlanetary Network, J-GEM, La Silla-QUEST Survey, Liverpool Telescope, LOFAR, MASTER, MAXI, MWA, Pan-STARRS, PESSTO, Pi of the Sky, SkyMapper, Swift, C2PU, TOROS, and VISTA Collaborations), Astrophys. J. Lett. **826**, L13 (2016).

[25] M. Aghaei Abchouyeh, M. H. P. M. van Putten, and L. Amati, Astrophys. J. **952**, 157 (2023).

[26] B. P. Abbott *et al.* (LIGO Scientific, Virgo, Fermi GBM, INTEGRAL, IceCube, AstroSat Cadmium Zinc Telluride Imager Team, IPN, Insight-Hxmt, ANTARES, Swift,

AGILE Team, 1M2H Team, Dark Energy Camera GW-EM, DES, DLT40, GRAWITA, Fermi-LAT, ATCA, AS-KAP, Las Cumbres Observatory Group, OzGrav, DWF (Deeper Wider Faster Program), AST3, CAASTRO, VINROUGE, MASTER, J-GEM, GROWTH, JAGWAR, CaltechNRAO, TTU-NRAO, NuSTAR, Pan-STARRS, MAXI Team, TZAC Consortium, KU, Nordic Optical Telescope, ePESSTO, GROND, Texas Tech University, SALT Group, TOROS, BOOTES, MWA, CALET, IKI-GW Follow-up, H.E.S.S., LOFAR, LWA, HAWC, Pierre Auger, ALMA, Euro VLBI Team, Pi of Sky, Chandra Team at McGill University, DFN, ATLAS Telescopes, High Time Resolution Universe Survey, RIMAS, RATIR, and SKA South Africa/MeerKAT Collaborations), Astrophys. J. Lett. **848,** L12 (2017).

[27] B. P. Abbott *et al.* (LIGO Scientific, Virgo, Fermi-GBM, and INTEGRAL Collaborations), Astrophys. J. Lett. **848,** L13 (2017).

[28] T. Dietrich, M. W. Coughlin, P. T. H. Pang, M. Bulla, J. Heinzel, L. Issa, I. Tews, and S. Antier, Science **370,** 1450 (2020).

[29] M. Bulla, M. W. Coughlin, S. Dhawan, and T. Dietrich, Universe **8,** 289 (2022).

[30] D. Kasen, B. Metzger, J. Barnes, E. Quataert, and E. Ramirez-Ruiz, Nature (London) **551,** 80 (2017).

[31] M. R. Drout *et al.*, Science **358,** 1570 (2017).

[32] B. P. Abbott *et al.* (LIGO Scientific and Virgo Collaborations), Phys. Rev. Lett. **119,** 141101 (2017).

[33] H. Koehn *et al.*, An overview of existing and new nuclear and astrophysical constraints on the equation of state of neutron-rich dense matter, Report No. lA-UR-24-20420, 2024, arXiv:2402.04172.

[34] I. Bartos, B. Kocsis, Z. Haiman, and S. Márka, Astrophys. J. **835,** 165 (2017).

[35] M. J. Graham *et al.*, Phys. Rev. Lett. **124,** 251102 (2020).

[36] H. Tagawa, S. S. Kimura, Z. Haiman, R. Perna, and I. Bartos, Astrophys. J. **950,** 13 (2023).

[37] Z.-H. Zhou and K. Wang, Astrophys. J. Lett. **958,** L12 (2023).

[38] F. J. Masci *et al.*, Publ. Astron. Soc. Pac. **131,** 018003 (2018).

[39] M. J. Graham *et al.*, Publ. Astron. Soc. Pac. **131,** 078001 (2019).

[40] v. Ivezić *et al.* (LSST Collaboration), Astrophys. J. **873,** 111 (2019).

[41] P. A. Abell *et al.* (LSST Science, LSST Project Collaborations), LSST science book, version 2.0, Reports No. FERMILAB-TM-2495-A, No. SLAC-R-1031, 2009, arXiv:0912.0201.

[42] S. Nissanke, M. Kasliwal, and A. Georgieva, Astrophys. J. **767,** 124 (2013).

[43] P. Jaranowski, A. Krolak, K. D. Kokkotas, and G. Tsegas, Classical Quantum Gravity **13,** 1279 (1996).

[44] S. Fairhurst, New J. Phys. **11,** 123006 (2009); **13,** 069602 (E) (2011).

[45] S. Fairhurst, Classical Quantum Gravity **28,** 105021 (2011).

[46] C. P. L. Berry *et al.*, Astrophys. J. **804,** 114 (2015).

[47] M. Bailes *et al.*, arXiv:1912.06305.

[48] L. Wen and Y. Chen, Phys. Rev. D **81,** 082001 (2010).

[49] S. Klimenko, G. Vedovato, M. Drago, G. Mazzolo, G. Mitselmakher, C. Pankow, G. Prodi, V. Re, F. Salemi, and I. Yakushin, Phys. Rev. D **83,** 102001 (2011).

[50] J. Veitch, I. Mandel, B. Aylott, B. Farr, V. Raymond, C. Rodriguez, M. van der Sluys, V. Kalogera, and A. Vecchio, Phys. Rev. D **85,** 104045 (2012).

[51] B. P. Abbott *et al.* (KAGRA, LIGO Scientific, Virgo Collaborations), Living Rev. Relativity **21,** 3 (2018).

[52] C. Pankow, E. A. Chase, S. Coughlin, M. Zevin, and V. Kalogera, Astrophys. J. Lett. **854,** L25 (2018).

[53] C. Pankow, M. Rizzo, K. Rao, C. P. L. Berry, and V. Kalogera, Astrophys. J. **902,** 71 (2020).

[54] S. R. Shukla, L. Pathak, and A. S. Sengupta, Phys. Rev. D **109,** 044051 (2024).

[55] L. P. Singer *et al.*, Astrophys. J. **795,** 105 (2014).

[56] R. Weiss *et al.*, LIGO Document No. t1000251-v1, 2010, https://dcc.ligo.org/public/0011/T1000251/001/committee_report_final.pdf.

[57] P. Raffai, L. Gondán, I. S. Heng, N. Kelecsényi, J. Logue, Z. Márka, and S. Márka, Classical Quantum Gravity **30,** 155004 (2013).

[58] W. Zhao and L. Wen, Phys. Rev. D **97,** 064031 (2018).

[59] E. D. Hall and M. Evans, Classical Quantum Gravity **36,** 225002 (2019).

[60] Y. Guersel and M. Tinto, Phys. Rev. D **40,** 3884 (1989).

[61] N. Arnaud, M. Barsuglia, M.-A. Bizouard, V. Brisson, F. Cavalier, M. Davier, P. Hello, S. Kreckelbergh, and E. K. Porter, Phys. Rev. D **68,** 102001 (2003).

[62] S. Klimenko, I. Yakushin, A. Mercer, and G. Mitselmakher, Classical Quantum Gravity **25,** 114029 (2008).

[63] N. J. Cornish and T. B. Littenberg, Classical Quantum Gravity **32,** 135012 (2015).

[64] S. Klimenko *et al.*, Phys. Rev. D **93,** 042004 (2016).

[65] H. Abe *et al.* (KAGRA Collaboration), Galaxies **10,** 63 (2022).

[66] LIGO Scientific Collaboration, LIGO observer documentation (2023), accessed on 24/1/2024.

[67] M. Dominik, E. Berti, R. O'Shaughnessy, I. Mandel, K. Belczynski, C. Fryer, D. E. Holz, T. Bulik, and F. Pannarale, Astrophys. J. **806,** 263 (2015).

[68] C. J. Neijssel, A. Vigna-Gómez, S. Stevenson, J. W. Barrett, S. M. Gaebel, F. Broekgaarden, S. E. de Mink, D. Szécsi, S. Vinciguerra, and I. Mandel, Mon. Not. R. Astron. Soc. **490,** 3740 (2019).

[69] P. Marchant, K. M. W. Pappas, M. Gallegos-Garcia, C. P. L. Berry, R. E. Taam, V. Kalogera, and P. Podsiadlowski, Astron. Astrophys. **650,** A107 (2021).

[70] M. Zevin, S. S. Bavera, C. P. L. Berry, V. Kalogera, T. Fragos, P. Marchant, C. L. Rodriguez, F. Antonini, D. E. Holz, and C. Pankow, Astrophys. J. **910,** 152 (2021).

[71] R. Abbott *et al.* (LIGO Scientific and Virgo Collaborations), Phys. Rev. D **102,** 043015 (2020).

[72] R. Abbott *et al.* (LIGO Scientific and Virgo Collaborations), Astrophys. J. Lett. **896,** L44 (2020).

[73] R. Abbott *et al.* (LIGO Scientific and Virgo Collaborations), Phys. Rev. Lett. **125,** 101102 (2020).

[74] R. Abbott *et al.* (LIGO Scientific and Virgo Collaborations), Astrophys. J. Lett. **900,** L13 (2020).

[75] R. Abbott *et al.* (KAGRA, Virgo, and LIGO Scientific Collaborations), Phys. Rev. X **13**, 041039 (2023).

[76] M. Hannam *et al.*, Nature (London) **610**, 652 (2022).

[77] A. Olejak, M. Fishbach, K. Belczynski, D. E. Holz, J. P. Lasota, M. C. Miller, and T. Bulik, Astrophys. J. Lett. **901**, L39 (2020).

[78] G. Fragione, E. Grishin, N. W. C. Leigh, H. B. Perets, and R. Perna, Mon. Not. R. Astron. Soc. **488**, 47 (2019).

[79] H. Tagawa, Z. Haiman, and B. Kocsis, Astrophys. J. **898**, 25 (2020).

[80] G. Fragione and B. Kocsis, Mon. Not. R. Astron. Soc. **486**, 4781 (2019).

[81] A. Vigna-Gómez, S. Toonen, E. Ramirez-Ruiz, N. W. C. Leigh, J. Riley, and C.-J. Haster, Astrophys. J. Lett. **907**, L19 (2021).

[82] I. Mandel and S. E. de Mink, Mon. Not. R. Astron. Soc. **458**, 2634 (2016).

[83] S. E. de Mink and I. Mandel, Mon. Not. R. Astron. Soc. **460**, 3545 (2016).

[84] L. du Buisson, P. Marchant, P. Podsiadlowski, C. Kobayashi, F. B. Abdalla, P. Taylor, I. Mandel, S. E. de Mink, T. J. Moriya, and N. Langer, Mon. Not. R. Astron. Soc. **499**, 5941 (2020).

[85] M. Colleoni, M. Mateu-Lucena, H. Estellés, C. García-Quirós, D. Keitel, G. Pratten, A. Ramos-Buades, and S. Husa, Phys. Rev. D **103**, 024029 (2021).

[86] G. Pratten, P. Schmidt, R. Buscicchio, and L. M. Thomas, Phys. Rev. Res. **2**, 043096 (2020).

[87] A. Ramos-Buades, A. Buonanno, H. Estellés, M. Khalil, D. P. Mihaylov, S. Ossokine, L. Pompili, and M. Shiferaw, Phys. Rev. D **108**, 124037 (2023).

[88] J. E. Thompson, E. Hamilton, L. London, S. Ghosh, P. Kolitsidou, C. Hoy, and M. Hannam, Phys. Rev. D **109**, 063012 (2024).

[89] A. Dhani, S. Völkel, A. Buonanno, H. Estelles, J. Gair, H. P. Pfeiffer, L. Pompili, and A. Toubiana, arXiv:2404.05811.

[90] A. Vecchio, Phys. Rev. D **70**, 042001 (2004).

[91] R. N. Lang and S. A. Hughes, Phys. Rev. D **74**, 122001 (2006); **75**, 089902(E) (2007); **77**, 109901(E) (2008).

[92] S. Vitale, R. Lynch, J. Veitch, V. Raymond, and R. Sturani, Phys. Rev. Lett. **112**, 251101 (2014).

[93] R. Green, C. Hoy, S. Fairhurst, M. Hannam, F. Pannarale, and C. Thomas, Phys. Rev. D **103**, 124023 (2021).

[94] L. S. Finn and D. F. Chernoff, Phys. Rev. D **47**, 2198 (1993).

[95] D. Davis *et al.* (LIGO Collaboration), Classical Quantum Gravity **38**, 135014 (2021).

[96] A. H. Nitz, T. Dent, G. S. Davies, and I. Harry, Astrophys. J. **897**, 169 (2020).

[97] B. P. Abbott *et al.* (LIGO Scientific and Virgo Collaborations), Classical Quantum Gravity **37**, 055002 (2020).

[98] H.-Y. Chen, D. E. Holz, J. Miller, M. Evans, S. Vitale, and J. Creighton, Classical Quantum Gravity **38**, 055010 (2021).

[99] H. Abe *et al.* (KAGRA Collaboration), Prog. Theor. Exp. Phys. **2023**, 10A101 (2023).

[100] F. Acernese *et al.* (Virgo Collaboration), J. Phys. Conf. Ser. **2429**, 012040 (2023).

[101] B. Willke *et al.*, Classical Quantum Gravity **19**, 1377 (2002).

[102] G. Ashton *et al.*, Astrophys. J. Suppl. Ser. **241**, 27 (2019).

[103] I. M. Romero-Shaw *et al.*, Mon. Not. R. Astron. Soc. **499**, 3295 (2020).

[104] LIGO Scientific Collaboration, LIGO Algorithm Library— LALSuite, free software (GPL) (2018).

[105] G. Pratten, S. Husa, C. Garcia-Quiros, M. Colleoni, A. Ramos-Buades, H. Estelles, and R. Jaume, Phys. Rev. D **102**, 064001 (2020).

[106] P. Whittle, *Hypothesis Testing in Time Series Analysis* (Almqvist & Wiksells Boktryckeri, Uppsala 1951), https://www.jstor.org/stable/2332487?origin=crossref.

[107] J. S. Speagle, Mon. Not. R. Astron. Soc. **493**, 3132 (2020).

[108] J. Skilling, AIP Conf. Proc. **735**, 395 (2004).

[109] LIGO/Virgo Skymap Software, https://lscsoft.docs.ligo.org/ligo.skymap/ (2022), accessed: December 10, 2022.

[110] F. Pedregosa, G. Varoquaux, A. Gramfort, V. Michel, B. Thirion, O. Grisel, M. Blondel, P. Prettenhofer, R. Weiss, V. Dubourg, J. Vanderplas, A. Passos, D. Cournapeau, M. Brucher, M. Perrot, and E. Duchesnay, J. Mach. Learn. Res. **12**, 2825 (2011), https://jmlr.csail.mit.edu/papers/v12/pedregosa11a.html.

[111] G. Pratten *et al.*, Phys. Rev. D **103**, 104056 (2021).

[112] B. P. Abbott *et al.* (Virgo and LIGO Scientific Collaborations), Phys. Rev. Lett. **119**, 161101 (2017).

[113] M. Hannam, P. Schmidt, A. Bohé, L. Haegel, S. Husa, F. Ohme, G. Pratten, and M. Pürrer, Phys. Rev. Lett. **113**, 151101 (2014).

[114] P. Canizares, S. E. Field, J. R. Gair, and M. Tiglio, Phys. Rev. D **87**, 124005 (2013).

[115] S. S. Bavera, T. Fragos, Y. Qin, E. Zapartas, C. J. Neijssel, I. Mandel, A. Batta, S. M. Gaebel, C. Kimball, and S. Stevenson, Astron. Astrophys. **635**, A97 (2020).

[116] P. Schmidt, M. Hannam, and S. Husa, Phys. Rev. D **86**, 104063 (2012).

[117] R. C. P. Casella George and W. M. T., IMS Lect. Notes Monogr. Ser. **45**, 342 (2004).

[118] P. C. Peters and J. Mathews, Phys. Rev. **131**, 435 (1963).

[119] V. Villa-Ortega, T. Dent, and A. C. Barroso, Mon. Not. R. Astron. Soc. **515**, 5718 (2022).

[120] L. S. Finn, Phys. Rev. D **46**, 5236 (1992).

[121] J. Veitch *et al.*, Phys. Rev. D **91**, 042003 (2015).

[122] B. P. Abbott *et al.* (Virgo and LIGO Scientific Collaborations), Phys. Rev. Lett. **116**, 241102 (2016).

[123] D. Davis, T. B. Littenberg, I. M. Romero-Shaw, M. Millhouse, J. McIver, F. Di Renzo, and G. Ashton, Classical Quantum Gravity **39**, 245013 (2022).

[124] B. P. Abbott *et al.* (LIGO Scientific and Virgo Collaborations), Astrophys. J. Lett. **892**, L3 (2020).

[125] T. Dal Canton and I. W. Harry, Designing a template bank to observe compact binary coalescences in Advanced LIGO's second observing run, Report No. lIGO-P1700085, 2017, arXiv:1705.01845.

[126] F. Beauville *et al.* (Virgo LIGO/Working Group), Classical Quantum Gravity **25**, 045001 (2008).

[127] R. Abbott *et al.* (KAGRA, Virgo, and LIGO Scientific Collaborations), Astrophys. J. Suppl. Ser. **267**, 29 (2023).